

Signatures of extended discs and outflows in the circumgalactic medium using the Q0107 quasar triplet

Alexander Beckett¹,¹★ Simon L. Morris¹, Michele Fumagalli^{2,3}, Nicolas Tejos⁴, Buell Jannuzi⁵ and Sebastiano Cantalupo²

¹Centre for Extragalactic Astronomy, Durham University, South Road, Durham DH1 3LE, UK

²Dipartimento di Fisica G. Occhialini, Università degli Studi di Milano Bicocca, Piazza della Scienza 3, I-20126 Milano, Italy

³INAF – Osservatorio Astronomico di Trieste, via G. B. Tiepolo 11, I-34143 Trieste, Italy

⁴Instituto de Física, Pontificia Universidad Católica de Valparaíso, Casilla, 4059 Valparaíso, Chile

⁵Steward Observatory, University of Arizona, 933 North Cherry Avenue, Tucson, AZ 85721, USA

Accepted 2022 September 1. Received 2022 August 31; in original form 2022 May 19

ABSTRACT

We use H I absorption along the lines-of-sight to the Q0107 quasar triplet in order to model potential disc and outflow structures in the circumgalactic medium of intervening galaxies at $z \lesssim 1$, as well as the intergalactic medium on scales of up to a few virial radii. We consider a sample of twelve isolated galaxies in the Q0107 field with position angles and inclinations measured from *HST* imaging as well as redshifts from our spectroscopic surveys, alongside 27 detected Ly α absorbers within 500 km s⁻¹ of these galaxies. Building on previous work showing increased incidence of absorption close to the projected major and minor axes, we use model rotating discs and bi-conical outflows in attempting to reproduce the observed absorption. Requiring these models to match absorption in multiple lines-of-sight provides additional constraints over single-sightline observations. We identify four possible outflows with velocities ~ 100 km s⁻¹, two of which extend to or beyond the virial radius, with a variety of opening angles. Two galaxies have nearby co-rotating absorbers with rotation velocities $\lesssim v_{\text{vir}}$, that may probe disc-like structures, and we can rule out a disc/outflow origin for a further ten absorbers. These indicate that outflowing and co-rotating structures can extend to large scales but are either not ubiquitous, or do not always produce detectable Ly α . In some cases, disc models are successful even close to the minor axis of the galaxy, and some of our model outflows exhibit wide opening angles. These results imply that purely geometrical cuts are not sufficient to distinguish between discs and outflows in single line-of-sight studies.

Key words: galaxies: evolution – intergalactic medium – quasars: absorption lines.

1 INTRODUCTION

The circumgalactic medium (CGM) is the reservoir of gas surrounding galaxies. Consisting of material outside the galaxy itself, but within its dark matter halo, it is often defined as extending to the virial radius (e.g. Tumlinson, Peebles & Werk 2017). Observations using absorption in the line-of-sight to background sources (often quasars) have long been used to study the gaseous haloes around intervening galaxies and the surrounding intergalactic medium (e.g. Bahcall & Spitzer 1969; Bergeron 1986; Bergeron et al. 1994; Weymann et al. 1998; Adelberger et al. 2005; Prochaska et al. 2011; Kacprzak, Churchill & Nielsen 2012b; Rubin et al. 2018; Pointon et al. 2019; Dutta et al. 2021; Wilde et al. 2021). The wide variance of absorber properties indicate a complex, multiphase medium (e.g. Tripp et al. 2008; Werk et al. 2013; Mathes et al. 2014; Péroux et al. 2019; Chen et al. 2020), but most of these studies can probe only a single line-of-sight through the CGM of any one galaxy, preventing detailed study of the CGM of each galaxy and limiting these works to statistical

properties of a sample of galaxy–sightline pairs. More information can be obtained by using multiple lines-of-sight where possible, although this requires rare cases with multiple closely spaced quasars (e.g. Fossati et al. 2019b; Maitra et al. 2019), sufficiently bright background galaxies (e.g. Zabl et al. 2020), multiply lensed quasars (e.g. Zahedy et al. 2016; Okoshi et al. 2021), or gravitational arcs (e.g. Lopez et al. 2018, 2020; Mortensen et al. 2021; Tejos et al. 2021).

The evolution of galaxies is strongly linked to the state of the CGM, with models suggesting that material ejected from the galaxy in stellar-wind-driven and AGN-driven outflows alongside material accreting on to the central galaxy regulates its star formation (e.g. Lehnert et al. 2013; Somerville, Popping & Trager 2015; Salcido, Bower & Theuns 2020). This exchange of material also transfers angular momentum between the galaxy and its CGM (e.g. Brook et al. 2012; DeFelippis et al. 2017, 2020; Stewart et al. 2017), which likely affects galaxy morphologies (e.g. Swinbank et al. 2017).

At distances of tens of kpc, observations of the cool gas in the $z \lesssim 1$ CGM often find a bimodality in the distribution of azimuthal angles, identified with outflows near to galaxy minor axes, and rotation and accretion along the major axis (e.g. Bouché et al. 2012; Kacprzak

* E-mail: alexander.beckett@durham.ac.uk

et al. 2012b; Zabl et al. 2019; Beckett et al. 2021). This difference in gas properties found at different azimuthal angles is also reproduced by many simulations (e.g. DeFelippis et al. 2020; Péroux et al. 2020; Hopkins et al. 2021).

Emission-line kinematics provide evidence for minor axis outflows, with early H α measurements of the wind from the nearby M82 (e.g. Bland & Tully 1988; Lehnert, Heckman & Weaver 1999) and other nearby galaxies (e.g. Heckman, Armus & Miley 1990), as well as more recent studies (e.g. Wang et al. 2020) and metal-line emission using integral field units such as MUSE and KCWI (e.g. Finley et al. 2017; Burchett et al. 2021; Zabl et al. 2021). Transverse and down-the-barrel absorption measurements also indicate cool outflowing material in transitions from H I and low metal ions such as Na I and Mg II (e.g. Lan & Mo 2018; Concas et al. 2019; Schroetter et al. 2019). Despite differing methods of energy injection representing stellar and AGN feedback, bi-conical outflows near the galaxy minor axis are found in many simulations, including EAGLE (e.g. Mitchell et al. 2020a), Illustris TNG50 (e.g. Nelson et al. 2019), and FIRE-2 (e.g. Hopkins et al. 2021).

Near the major axis, evidence for co-rotation has been found using a similarly wide range of diagnostics, including absorption in H I (e.g. Bouché et al. 2016; French & Wakker 2020) and Mg II (e.g. Charlton & Churchill 1998; Steidel et al. 2002; Ho et al. 2017; Martin et al. 2019; Zabl et al. 2019; Tejos et al. 2021), as well as Mg II emission (Leclercq et al. 2022). Again, down-the-barrel measurements have found examples of infalling material (e.g. Rubin et al. 2012), and disc-like models have been used for X-ray emission from the CGM of the Milky Way (Kaaret et al. 2020) and absorption around NGC 1097 (Bowen et al. 2016). Simulations also find that the cool CGM forms co-rotating and accreting flows near the galaxy major axis (e.g. DeFelippis et al. 2020; Ho, Martin & Schaye 2020).

Whilst these structures are common to most models and are deduced from a variety of observations, there remains uncertainty on several fronts. First, Hopkins et al. (2021) add cosmic rays to the driving of outflows in the FIRE simulations, which allows them to reach megaparsec scales around L_* galaxies, whereas the outflow rates without cosmic rays, and those in Illustris for most stellar masses (Nelson et al. 2019), drop dramatically beyond 50 kpc. It is also unclear how much cool gas is contained within these winds, with some models suggesting primarily hot winds (e.g. Pandya et al. 2021), and others allowing cool winds to large scales (e.g. Fielding & Bryan 2022).

The extent of the cool, co-rotating structures in the CGM is also not well-determined. The FIRE simulations suggest that gas infall on to galaxies is primarily hot at distances above ≈ 40 kpc for L_* (Hafen et al. 2022), and hot accretion is generally expected to dominate around such galaxies at low redshift (e.g. Faucher-Giguère, Kereš & Ma 2011; Fielding et al. 2017), yet predictions and detections of co-rotating cool gas (often in the form of Mg II) extend substantially further (e.g. Zabl et al. 2019; French & Wakker 2020; Ho et al. 2020).

Robustly determining whether absorption measurements are probing these structures is extremely difficult using single-sightline observations, with some studies selecting candidate outflow and disc absorbers based on galaxy inclination and absorber azimuthal angle (e.g. Bordoloi et al. 2011; Schroetter et al. 2015, 2019; Zabl et al. 2019). Improving upon this selection strategy will require multiple lines-of-sight probing a range of impact parameters around the same galaxy.

In this study we focus on the Q0107 system, a quasar triplet at $z \sim 1$: LBQS 0107-025A, LBQS 0107-025B, and LBQS 0107-0232, hereafter denoted A, B, and C. QSOs A and B lie at $z \approx 0.96$, with C at $z \approx 0.73$, with co-ordinates given in Table 1. The three quasars have

Table 1. Co-ordinates, redshifts, and R -band magnitudes of the three quasars used as background sources in this study.

Object	RA (J2000)	Dec (J2000)	Redshift	R -mag
Q0107-025 A	01:10:13.14	-2:19:52.9	0.960	18.1
Q0107-025 B	01:10:16.25	-2:18:51.0	0.956	17.4
Q0107-0232 (C)	01:10:14.43	-2:16:57.6	0.726	18.4

separations of ≈ 1 arcmin (≈ 370 kpc at $z=0.5$), allowing multiple lines-of-sight to be probed through the CGM/IGM around galaxies in this field. Ly α absorption along these sightlines allows a combination of lower column densities and larger scales than most studies relying on gravitationally lensed systems (arcs or multiply lensed QSOs, e.g. Zahedy et al. 2016; Lopez et al. 2018; Mortensen et al. 2021; Okoshi et al. 2021; Tejos et al. 2021).

Many studies have utilized this unique configuration to study the gas around galaxies. Dinshaw et al. (1997) observed QSOs A and B, using a maximum-likelihood analysis to conclude that the data were best explained by randomly inclined discs approximately 1 Mpc in radius. A larger sample including the Q0107-A and B pair was analysed in D’Odorico et al. (1998), who concluded a disc-like or spherical geometry was possible, with radii ≈ 600 kpc. Young, Impey & Foltz (2001) complemented this by considering absorption systems appearing in multiple sightlines at similar redshifts, and found that matches involving stronger absorption tended to have smaller velocity separations. Such systems also occur more frequently among high-column-density absorbers, as found by Petry et al. (2006).

Crighton et al. (2010) used improved QSO spectra of all three lines-of-sight as well as galaxy spectra. They observed a highly significant excess of absorption systems covering all three sightlines over an ensemble of randoms, providing clear evidence that gas and galaxies are associated on scales of hundreds of kpc. This field was also included in studies of galaxy-absorber cross-correlations in H I (Tejos et al. 2014, hereafter T14) and O VI (Finn et al. 2016).

Absorbers detected in more than one of these three lines-of-sight at a similar redshift have also been studied in detail using ionization modelling. Muzahid (2014) detected both the warm and cool phase of the CGM around an L_* galaxy at $z \approx 0.2$, whilst Anshul et al. (2021) detected multiphase gas at $z \approx 0.4$.

We built on these works in Beckett et al. (2021), hereafter Paper 1, in which we showed that the excess absorption seen covering multiple lines-of-sight separated by hundreds of kpc is stronger both in high-column-density absorption and around star-forming galaxies, than in low-density absorption and around quiescent galaxies. We found a bimodality in the distribution of azimuthal angles of detected galaxy-absorber pairs, extending to ≈ 300 kpc. That absorbers near the major axis had line-of-sight velocities preferentially aligned with the galaxy rotation and that minor axis absorbers were more likely to exhibit O VI suggest that the higher detection rates near the major and minor axes are due to rotating and outflowing structures, respectively.

In this paper, we model the absorption around galaxies in the Q0107 field in order to test for these structures in the CGM. The presence of multiple lines-of-sight through the Q0107 field, alongside the extensive galaxy data, constrains the model absorption at multiple locations around the galaxy. We can therefore determine the CGM structures probed by our sightlines more confidently than in single-sightline observations.

At redshifts with multiple galaxies near to the lines-of-sight, we might expect tidal debris (e.g. Morris & van den Bergh 1994), ram-pressure-stripped gas (e.g. Fumagalli et al. 2014; Fossati et al. 2019a), and other intragroup material (e.g. Stocke et al. 2014; Bielby

Table 2. Summary of galaxy properties for our selected sample of isolated galaxies. Derivation of these properties is described in more detail in [Paper 1](#). Column descriptions: (1) Galaxy ID used in this work (MUSE and MOS IDs were collated separately; MUSE ID is used for galaxies featuring in both MOS and MUSE catalogues); (2) galaxy redshift (all galaxies in this subsample have redshift uncertainties smaller than 0.001); (3, 4) on-sky coordinates of galaxy; (5) observed magnitude in the SDSS r -band; (6) galaxy luminosity in SDSS r -band as a multiple of L_* (L_* estimate from [Montero-Dorta & Prada \(2009\)](#), uncertainties smaller than $0.005 L_*$ are omitted); (7) stellar mass estimated as in [Johnson, Chen & Mulchaey \(2015\)](#) (for most galaxies the largest uncertainty is a scatter of 0.15 dex in their relation); (8) halo mass estimated using the abundance matching technique from [Behroozi, Conroy & Wechsler \(2010\)](#); (9) star-formation flag denoting a star-forming or non-star-forming galaxy; (10) star-formation rate estimated from galaxy emission lines, using the [Kennicutt \(1998\)](#) and [Kewley, Geller & Jansen \(2004\)](#) calibrations for $H\alpha$ and $[O II]$, respectively (uncertainties are a combination of scatter in these relationships and uncertainty in the line fit); (11) line used to estimate SFR (SFRs estimated from $H\beta$ using the correlation between SFR estimated from $H\alpha$ and $H\beta$ line luminosity, generating a substantially larger uncertainty); (12) note of whether emission-line kinematics from the MUSE data are available for this galaxy.

Galaxy	z	RA ◦	Dec ◦	r -band	Luminosity (L_*)	M_* $\log_{10}(M_{\odot})$	M_h $\log_{10}(M_{\odot})$	SF Flag	SFR ($M_{\odot} \text{ yr}^{-1}$)	Line	Kinematics
(1)	(2)	(3)	(4)	(5)	(6)	(7)	(8)	(9)	(10)	(11)	(12)
A-14	0.053	17.5594	-2.3363	19.93 ± 0.01	0.02	8.7 ± 0.2	10.9 ± 0.3	SF	$0.018^{+0.009}_{-0.006}$	$H\alpha$	Yes
26732	0.087	17.5576	-2.3466	22.80 ± 0.02	0.01	7.4 ± 0.2	10.4 ± 0.3	SF	$0.016^{+0.007}_{-0.005}$	$H\alpha$	No
25833	0.123	17.5631	-2.3591	19.83 ± 0.01	0.10	9.7 ± 0.2	11.4 ± 0.3	non-SF	<0.06	$H\alpha$	No
A-62	0.178	17.5569	-2.3280	21.78 ± 0.01	0.04	8.7 ± 0.2	11.0 ± 0.3	SF	$0.23^{+0.16}_{-0.09}$	$H\alpha$	Poor
A-65	0.220	17.5522	-2.3265	26.06 ± 0.46	0.01	7.6 ± 0.7	10.5 ± 0.7	SF	$0.012^{+0.005}_{-0.003}$	$H\alpha$	No
B-14	0.261	17.5720	-2.3200	22.57 ± 0.02	0.05	8.5 ± 0.2	10.9 ± 0.3	SF	$6.3^{+3.3}_{-2.2}$	$H\alpha$	Yes
A-63	0.488	17.5598	-2.3274	23.38 ± 0.03	0.09	9.6 ± 0.2	11.5 ± 0.3	SF	$0.25^{+0.63}_{-0.18}$	$H\beta$	Yes
30169	0.584	17.5337	-2.3138	21.65 ± 0.01	0.68 ± 0.02	9.8 ± 0.2	11.6 ± 0.3	SF	$4.0^{+10.0}_{-2.9}$	$H\beta$	No
31658	0.728	17.5536	-2.2966	22.81 ± 0.03	0.40 ± 0.02	10.6 ± 0.2	12.4 ± 0.6	SF	$7.1^{+2.3}_{-1.8}$	$[O II]$	No
A-23	0.843	17.5626	-2.3339	23.86 ± 0.12	0.22 ± 0.03	10.7 ± 0.3	12.5 ± 0.7	SF	$2.7^{+0.9}_{-0.7}$	$[O II]$	Poor
A-30	0.850	17.5545	-2.3327	24.58 ± 0.21	0.12 ± 0.02	10.7 ± 0.3	12.5 ± 0.7	non-SF	$0.25^{+0.14}_{-0.09}$	$[O II]$	Poor
A-64	0.926	17.5523	-2.3272	24.58 ± 0.03	0.14 ± 0.03	10.4 ± 0.5	12.1 ± 0.8	SF	$1.8^{+0.6}_{-0.5}$	$[O II]$	Yes

et al. 2017; Péroux et al. 2017), as well as distortion of any disc or outflow structures in the CGM. We therefore consider only isolated galaxies here, deferring analysis of galaxies that are not isolated to a later work. For the purposes of this paper, we select galaxies with no detected companion within 500 kpc and 500 km s^{-1} . This is substantially larger than the virial radius and velocity for the galaxies in our sample, allowing us to test for the presence of outflows near the CGM/IGM interface.¹ This rules out group interactions as far as possible given our detection limits, but does not rule out a contribution from faint undetected galaxies.

In Section 2 we summarize the data used in this study, discussed more extensively in [Paper 1](#) and references therein, as well as selection of the subsample of isolated galaxies considered in this work. Section 3 summarizes the toy models used in our attempts to reproduce the observed absorption, whilst Section 4 describes in detail three example galaxies and their surrounding absorption. We then discuss the results from our sample in Section 5, and finally summarize in Section 6. Details of the modelling process and the results from the remainder of our galaxy sample are left to the appendices.

We use the Planck 2018 cosmology ([Planck Collaboration VI 2020](#)) throughout, with $\Omega_m = 0.315$ and $H_0 = 67.4 \text{ km s}^{-1} \text{ Mpc}^{-1}$, and quote physical sizes and distances unless otherwise stated.

2 DATA

This paper makes use of the absorber and galaxy catalogues used in [Paper 1](#), built on those used in [T14](#). The data and reduction procedures used to generate these catalogues are described in more detail therein, but also summarized here.

¹We only consider galaxies with spectroscopic redshifts, as deep imaging for this field consists of too few bands for estimating photometric redshifts. Completeness is discussed briefly in Section 2 of this work, and more thoroughly in [Paper 1](#) and [T14](#).

2.1 IGM data

We make use of observations of the quasars in the far- and near-UV from the *Hubble Space Telescope*, using the Cosmic Origins Spectrograph (COS, [Green et al. 2012](#)) and Faint Object Spectrograph (FOS, respectively). The COS spectra were observed in 2010-11 (program GO-11585, PI: Neil Crighton), whilst the FOS data are described in [Young et al. \(2001\)](#). The observations are detailed in Table 2 of [Paper 1](#). These allow $\text{Ly}\alpha$ to be observed in each line-of-sight from $z=0$ to the redshift of the QSO. The G130M and G270H gratings are omitted for QSO-C, as a sub-damped $\text{Ly}\alpha$ system at $z \approx 0.56$ obscures any low- z $\text{Ly}\alpha$ in the shorter wavelength grating, and its lower redshift precludes $\text{Ly}\alpha$ from the longer wavelength grating.

We use the line catalogue from [T14](#) (also used by [F16](#) and [Paper 1](#)). They describe the data reduction process in more detail. Briefly, the data reduction used the standard CALCOS and CALFOS pipelines. The overlapping regions between gratings were compared to ensure that the wavelength scales were consistent across the wavelength range. A continuum level was found by fitting a cubic spline to 12 Å ‘chunks’ of the spectrum (after removing outliers), and then checking ‘by-eye’ to ensure a reasonable fit (see their fig. 1).

Absorption systems were identified using VPFIT ([Carswell & Webb 2014](#)), which estimated redshifts, line widths, and column densities. The signal-to-noise ratio of the COS spectra (using results from [Keeney et al. 2012](#)) are consistent with a 3σ detection limit estimate of $\sim 10^{13} \text{ cm}^{-2}$, which is also consistent with the $H I$ column density distribution of our sample. The lower resolution FOS spectra have a slightly higher detection limit, at $\sim 10^{13.5} \text{ cm}^{-2}$.

We note that IGM absorbers are primarily found with Doppler widths $> 20 \text{ km s}^{-1}$ (e.g. [Davé et al. 2010](#)), so most $\text{Ly}\alpha$ absorbers in the COS spectra below $z \approx 0.45$ are resolved. The poorer resolution in the FOS spectra will introduce unresolved and potentially blended absorption, although the absorption components can often be resolved by referring to higher order Lyman lines that still lie in the COS spectra.

The catalogue contains 430 absorption systems, of which 272 are H I.

2.2 Galaxy data

The galaxy data used in this study comes from a number of different surveys, with spectra from VIMOS, DEIMOS, GMOS, and CFHT-MOS observations (referred to as MOS data throughout), as well as more recent observations using the Multi-Unit Spectroscopic Explorer (MUSE; Bacon et al. 2010). There is also *Hubble Space Telescope* imaging of the field, used to determine inclinations and position angles of galaxies close to the lines-of-sight.

2.2.1 MOS data

The MOS galaxy data are the subset of the catalogue from T14 that covers the Q0107 field. Both Paper 1 and T14 (with references therein) describe the data collection and reduction processes in more detail. The multi-object spectrograph on the Canada–France–Hawaii Telescope (CFHT-MOS; Le Fevre et al. 1994) was used to observe 29 galaxies in the Q0107 field (described in Morris & Jannuzi 2006). The VIMOS data (Le Fevre et al. 2003) consist of 935 low-resolution ($R \sim 200$) spectra with coverage between 5500 and 9500 Å (programs 086.A-0970, PI: Crighton; and 087.A-0857, PI: Tejos), reduced using VIPGI (Scodreggio et al. 2005). The DEIMOS (Faber et al. 2003) data were taken in 2007–08, covering the 6400–9100 Å range for 642 objects (program A290D, PIs: Bechtold and Jannuzi). The DEEP2 data reduction pipeline (Newman et al. 2013) included redshift estimation, as well as all necessary de-biasing, flat-fielding, wavelength and flux calibration, and heliocentric corrections. 210 redshifts were estimated from GMOS (Davies et al. 1997) data, taken in 2008 (program GS-2008B-Q-50, PI: Crighton), with an intermediate resolving power ($R \sim 640$). Both VIMOS and GMOS redshifts required small redshift corrections in order to match the results from DEIMOS (chosen due to its higher resolution), of 0.0008 and 0.0004, respectively. Galaxy redshifts were assigned confidence flags of ‘a’ (highly confident), ‘b’ (good), and ‘c’ (uncertain). Only galaxies with ‘a’ and ‘b’ flags are included in our analysis.

2.2.2 MUSE data

MUSE GTO observations cover two 1 arcmin \times 1 arcmin fields of view around QSO-A and QSO-B (program ID 094.A-0131, PI Schaye). These cover the wavelength range from 4750 to 9350 Å with FWHM of ≈ 2.7 Å, and offer seeing of 0.96 arcsec for QSO-A, and 0.82 arcsec for QSO-B. These data are not only slightly deeper than the MOS surveys, but also provide galaxy kinematics for those close to the A or B sightlines.

We reduced the data using a similar process to many other studies (e.g. Fumagalli et al. 2016; Fossati et al. 2019b; Bielby et al. 2020; Lofthouse et al. 2020; Muzahid et al. 2021). MUSE ESO pipeline routines were used to remove bias, apply flat-fielding, calibrate astrometry and wavelength for each exposure, combine the IFUs for each exposure, and correct for telluric absorption using a basic sky model. We then use the CUBEX package (Cantalupo et al. 2019) to apply a renormalization between the different IFUs, stacks and slices, and an improved, flux-conserving sky subtraction. This reduces the ‘chequered’ pattern that often affects images reduced solely with the ESO pipeline, as well as reducing sky residuals.

SEXTRACTOR (Bertin & Arnouts 1996) was run on the MUSE white-light image to identify objects in the MUSE fields, and 1D spectra were produced by summing the flux within the SEXTRACTOR aperture (140 objects). We then used the MARZ software (Hinton et al. 2016) on these 1D spectra to estimate redshifts. Those identified as galaxies and with at least two identified spectral features were included in our combined galaxy catalogue (68 galaxies, 27 of which are also in the MOS catalogue).

2.2.3 Combined catalogue

The process of combining the MOS catalogues from T14 with the MUSE and *HST* data is described in full in Paper 1. Briefly, astrometry from bright objects in the MUSE and MOS fields was compared with objects in the SDSS catalogue (Albareti et al. 2017). The MUSE data required a small (< 1 arcsec) shift then objects within 1 arcsec were matched. Magnitudes were found to be consistent within the estimated uncertainties. The MUSE redshifts were found to be systematically higher than those in the MOS and absorber catalogues, requiring a shift of ≈ 30 km s $^{-1}$ to ensure consistency across our full samples. Some galaxies were observed multiple times with the same instrument, so the differences in the resulting redshift estimates were used to estimate redshift uncertainties. We estimated uncertainties separately for each instrument and redshift confidence flag. As the MUSE fields contain no duplicates, and GMOS has a slightly poorer resolution than MUSE, the redshift uncertainties found for GMOS were taken as a conservative estimate for MUSE galaxies.

This produces our final catalogue of 1424 galaxies, of which 1026 have ‘a’ or ‘b’ flags and were used in the analyses in Paper 1.

However, modelling the absorption arising from structures around galaxies requires good estimates of galaxy inclinations and position angles. We therefore use publicly available high-resolution imaging from the *Hubble Space Telescope* (Program ID: 14660, PI Straka), obtained with the ACS (Ryon 2019) and the F814W filter.

This covers a much larger field around the A and B quasars than the MUSE data (as seen in Fig. 1), but a much smaller field than the MOS surveys. As in our analysis of the MUSE data, galaxies in the *HST* image were identified using SEXTRACTOR, then matched to the coordinates of objects in our combined redshift catalogue. We found no systematic offset in the astrometry, so objects within 1 arcsec were matched.

GALFIT (Peng et al. 2002) was used to model all galaxies in the *HST*/ACS image that also had redshifts in our catalogue. This uses chi-squared minimization to produce a best-fitting model of a galaxy. We initially fit a Sersic disc to each galaxy, using the SEXTRACTOR results as initial guesses, and then introduced additional components where necessary to find a reasonable fit. This takes account of the point-spread function of the image, and is therefore able to reduce the average uncertainty in inclinations and position angles by a factor of ≈ 3 relative to the SEXTRACTOR results.

Galaxies for which the fit clearly failed to converge to a reasonable result were excluded. However, we do include galaxies that are near to face-on; these have large uncertainties in position angle that are discussed in each case. This returned 109 galaxies with position angle and inclination measurements as well as spectroscopic redshifts.

2.3 Galaxy sample selection

The majority of the 109 galaxies with both position angle/inclination measurements and redshifts lie in close proximity to multiple other

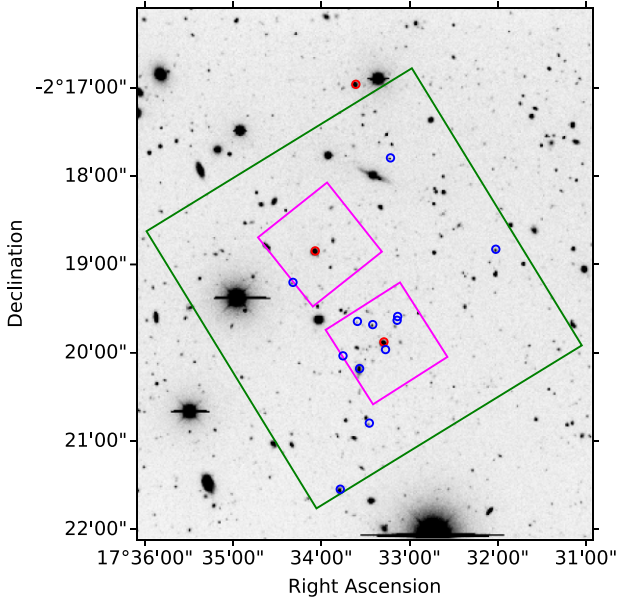


Figure 1. The layout of the surveys used in this study. The background image was taken with the Kitt Peak 4-m Telescope. The solid green square shows the region covered by *HST* imaging, whilst the smaller magenta squares show the MUSE fields centred on QSOs A and B. The quasars are shown by red circles, with A the southernmost and C the northernmost. The twelve galaxies included in our ‘isolated’ sample are shown with blue circles.

galaxies. We use a 500 kpc and 500 km s^{-1} cut in order to select isolated galaxies, so that their CGM is less likely to be disturbed by interactions with other galaxies. This produces a sample of 12 galaxies which we model in this paper. We note that this does not rule out the possibility of fainter galaxies for which we could not estimate a redshift either directly contributing to the absorption (e.g. Ho et al. 2020), or disturbing the CGM of the detected galaxy, nor does it rule out previous mergers leaving a disturbed CGM.

Galaxies are shown in relation to the quasar sightlines and the observations in Fig. 1, and several galaxy properties are listed in Table 2.

Fig. 2 shows these galaxies on the stellar mass–SFR plane alongside the full galaxy survey of this field. Most of the galaxies considered in this work lie close to the main sequence of star-forming galaxies, with two non-star-forming galaxies well below this (A-30 and 25833), and one galaxy substantially above the main sequence (B-14). The selected galaxies are biased towards low stellar masses and high star-formation rates relative to the full sample. This is because we only select galaxies within the *HST* field, which is the deepest part of the survey. The *HST* field also includes the MUSE data, from which faint emission-line galaxies can be detected.

3 MODELS

We use three basic toy models throughout this work: a biconical outflow, a rotating disc, and a power-law halo. Our models are described briefly here; further details are given in Appendix A. The parameters used to describe each of these models are listed in Table 3 and discussed here. These models are heavily dependent on the galaxy and sightline orientation, so impact parameter, galaxy inclination, and azimuthal angle are also inputs to these models, with values fixed by the observations rather than as free parameters.

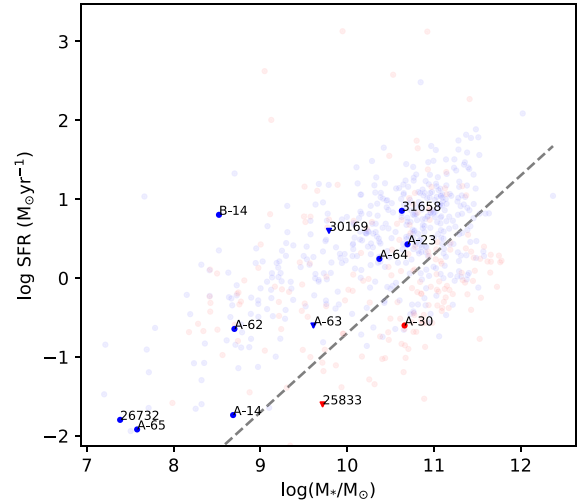


Figure 2. Stellar mass versus star-formation rate for galaxies in our sample. Faded points show the overall galaxy sample (identical to Fig. 5 from Paper 1), whilst galaxies detailed in this work are bold and labelled with the galaxy MOS or MUSE ID as given in Table 7. Galaxies identified as star-forming are shown in blue, with non-star-forming galaxies in red. The grey dashed line indicates an sSFR of 0.02 Gyr^{-1} , an approximate match to the SF/non-SF designations that were made using template fitting. Masses are estimated using the formulae from Johnson et al. (2015) and star-formation rates estimated using the $\text{H}\alpha$ or $[\text{O II}]$ (3727 \AA) luminosities. These measurements are detailed in Paper 1. Note that neither line is available for the three objects marked by triangles. They do not lie in the wavelength region covered by the spectra of A-63 and 30169, so the correlation between $\text{H}\alpha/[\text{O II}]$ SFR and $\text{H}\beta$ luminosity has been used, producing a large uncertainty. Galaxy 25833 is non-star-forming, so the noise in its spectrum has been used to generate an approximate upper limit.

Table 3. Summary of parameters describing the toy models used in this work.

Symbol	Description	Unit
Halo		
v_t	Thermal/turbulent velocity	km s^{-1}
ρ_1	Reference H I density (1 kpc)	cm^{-3}
α	Power law index (on H I density profile)	–
v_δ	Galaxy–Halo velocity offset	km s^{-1}
Outflow		
v_t	Thermal/turbulent velocity	km s^{-1}
ρ_1	Reference H I density (1 kpc)	cm^{-3}
v_{out}	Outflow velocity (constant)	km s^{-1}
θ_{out}	Half-opening angle	$^\circ$
θ_{in}	Inner half-opening angle	$^\circ$
S_{Nr}	Galaxy orientation	–
Disc		
v_t	Thermal/turbulent velocity	km s^{-1}
ρ_0	Reference H I density ($r = 0$)	cm^{-3}
h_r	Disc-plane scale height	kpc
h_z	‘Vertical’ scale height	kpc
v_r	Infall velocity	km s^{-1}
v_ϕ	Rotation velocity	km s^{-1}
S_{Nr}	Galaxy orientation	–
S_{Wr}	Direction of rotation	–

For our model outflows, we assume a constant velocity and constant flow rate, necessitating a r^{-2} density profile. An approximately constant outflow velocity (v_{out}) does appear to be justified by some simulations (e.g. Mitchell, Schaye & Bower 2020b), although TNG50 outflows appear to slow somewhat at small scales (over the first ≈ 20 kpc; Nelson et al. 2019). A well-defined opening angle is supported by observations, in nearby emission (Bland & Tully 1988), transverse absorption (e.g. Bordoloi et al. 2011), and down-the-barrel observations (Rubin et al. 2014), which we assume to be constant (we label the half-opening angle θ_{out}). We do allow for a hollow cone in which the centre of the outflow is further heated such that the neutral fraction is low and HI density is suppressed. Outside the cone (or in the centre of a hollow cone, where the polar angle $\theta < \theta_{\text{in}}$), we use a density of zero. Where multiple lines-of-sight probe an outflow, it may be possible to detect changes in velocity or opening angle with radius, but we do not attempt to quantify these in our toy models. Our galaxy observations cannot generally be used to distinguish which cone of the outflow is inclined away from us, so we use the S_{Nr} parameter, which has a value of +1 if the outflow cone to the north of the galaxy is moving redwards along the line-of-sight or -1 otherwise, to allow either case to be modelled.

Our model rotating discs are naturally constrained to the same direction as the galaxy kinematics (if visible), denoted by the S_{Wr} parameter which similarly has a value of ± 1 . They have exponential density profiles parallel and perpendicular to the major axis, with independent scale heights (h_r and h_z). In addition to the rotational velocity (v_ϕ), an accreting component of velocity is allowed (v_r), as in Zabl et al. (2020). A large vertical scale height would allow our models to be compatible with the thick disc suggested by Steidel et al. (2002), as well as the thick disc and ‘wedge’ seen in the simulated cool CGM by Ho et al. (2020) and DeFelippis et al. (2020). The scale heights we consider in our models can be constrained both by the column densities of absorption at different position angles, as well as absorber widths, although we do not model any lag in velocity with height, as considered in Steidel et al. (2002). The separate rotating and infalling velocity components can be constrained by differing velocity offsets at the locations of the lines-of-sight.

We also model a spherical halo with a power-law density profile (index α), and allow a small velocity offset between the halo and galaxy (v_s , allowing for actual peculiar velocity or the uncertainty on the redshift measurements). This requires absorbers at the same redshift with column densities that are larger in sightlines with smaller impact parameters.

All three model types require a reference density in order to set the strength of the model absorption. As the power-law profile is undefined at $r = 0$, we use the density at a radius of 1 kpc as the reference value (ρ_1) for both the halo and outflow models. The exponential density profile used for our model disc is well-defined at $r = 0$, so we use this density ρ_0 to normalize our model densities. The three model types also all allow for a thermal or turbulent velocity component v_t that can further widen any absorption features. (We do not attempt to distinguish between broadening due to thermal or turbulent velocities.) This term makes no noticeable difference to the broad absorbers seen using FOS, but we adopt values of 20–40 km s^{-1} to help to improve the fit for some resolved absorbers in the COS spectra. This is consistent with the expected widths of IGM absorbers (e.g. Davé et al. 2010).

We consider points at 10 pc intervals along the line-of-sight, and apply the following process:

(i) We convert the coordinates of these points from the observed (impact parameter, position angle, and distance along LOS) into the

relevant coordinates for the proposed model around the galaxy using the inclination and position angle estimates from the *HST* image.

(ii) Using the model parameters, we calculate the HI density and line-of-sight velocity component at each point. These values are applied to the entire 10-pc section centred at that point, from which we calculate the column density of that segment of the line-of-sight.

(iii) We use the properties of the Ly α transition to calculate the optical thickness of each 10-pc column section from the column density. This is then convolved with a Gaussian of width v_t , and binned by line-of-sight velocity (using bins of 0.25 km s^{-1}), producing model optical thickness as a function of velocity.

(iv) For systems in which the proposed model consists of multiple components (e.g. a both a disc and an outflow), we calculate the optical thickness separately and then sum the models together.

(v) Converting the optical thickness to transmission spectra and convolving with the relevant COS or FOS line-spread function produces our final model spectra.

Our model spectra can then be compared with the observations in all three lines-of-sight.

Whilst an automated fitting routine for quantifying the goodness-of-fit between the model and observed spectra and tuning the model parameters to find the best fit for each model type would allow our results to be more reliably reproduced, creating such a routine presents several difficulties. Absorption features known to be due to transitions other than Ly α would need to be masked. However, identifying which absorption features are due to Ly α is itself uncertain, and will affect the fit.

This routine would need to account for blended features, where a physical model might only provide a good fit to a small number of pixels in the spectrum. The likelihood function used would need to allow for blends, probably by penalizing model absorption that is weaker than observed to a lesser extent than model absorption that is stronger than that observed. Some form of weighting would also be needed to allow for the fact that absorbers with large velocity offsets and/or large impact parameters are more likely to be physically unconnected with the galaxy. Furthermore, models consisting of both discs and outflows would be difficult to constrain due to the much larger number of free parameters.

Tuning these weights in order to produce meaningful results would be arbitrary as well as time-consuming. For these reasons, we do not attempt an automated fit in this work, and instead vary the parameters manually until a reasonable fit is obtained.

For each galaxy, we consider each model type and combination of orientations (S_{Nr} and S_{Wr} , defined above), producing seven possible models. In most cases the halo model can be ruled out, as it requires the closest sightlines to exhibit the strongest absorption, and all absorbers to have small and similar velocity offsets to the galaxy. Several combinations of orientation can also be ruled out from producing any identified absorption components because the direction of galaxy–absorber velocity offset produced by the model is opposite to that seen in the observed spectra. Additionally, the galaxy kinematics constrain the direction of rotation (S_{Wr}) if a velocity gradient is visible.

With the model types and orientations greatly limited, we then identify the model velocities required to reproduce the observed offset between galaxy and an absorber (this is strongly dependent on the galaxy inclination), and adjust the density parameter to provide an approximate fit to the absorber (the total model column density is then usually consistent with the catalogue value estimated by VPFIT). If it is clear that reproducing this absorber introduces inconsistency with

Table 4. Summary of galaxies and absorbers at $z \sim 0.053$. Column descriptions: (1) Galaxy ID; (2) galaxy redshift; (3) galaxy luminosity as a multiple of L_* ; (4) galaxy inclination measured using GALFIT; (5) absorber line-of-sight; (6) impact parameter of absorber around galaxy; (7) azimuthal angle between absorber and galaxy major axis; (8) absorber column density; (9) absorber Doppler width; (10) velocity offset between galaxy and absorber (positive values denote absorbers ‘redwards’ of the galaxy); (11) any detected transitions at this redshift other than neutral hydrogen.

Galaxy (1)	z (2)	Lum (L_*) (3)	Inc (4)	LOS (5)	Imp (kpc) (6)	Azimuth (7)	$\log(N \text{ H I})$ (8)	b (km s^{-1}) (9)	Δv (km s^{-1}) (10)	Other ions (11)
A-14	0.053	0.02	$62^\circ \pm 1^\circ$	A	26	$38^\circ \pm 1^\circ$	13.67 ± 0.29	103 ± 50	-30 ± 60	–
–	–	–	–	A	26	$38^\circ \pm 1^\circ$	14.36 ± 0.09	36 ± 7	-40 ± 60	–
–	–	–	–	A	26	$38^\circ \pm 1^\circ$	13.31 ± 0.09	15 ± 6	-220 ± 60	–
–	–	–	–	B	91	$29^\circ \pm 1^\circ$	(None, limit ≈ 12.9)	–	–	–

absorption in the other lines-of-sight, then this model combination can also be discarded.

We then iteratively adjust the remaining parameters to improve the fit, matching the width of the absorber and ensuring that the model absorption in other sightlines is consistent with the observations where possible (usually either by reducing it to a level not distinguishable from the noise, or by matching another absorber). The absorber width depends on both v_t and the combination of velocities and opening angle/scale height, so models can often be ruled out at this stage.

Note that we do not artificially limit the range of values any parameters can take at this stage, although velocities are limited by the 500 km s^{-1} cut.

This process leads to a small number of possible models that can reproduce each absorber, or rules out all of our toy models. As long as the orientations are compatible (e.g. a disc and outflow existing around the same galaxy must have the same S_{Nr}), these can then be combined to fit as many absorption components as possible.

For the reasons stated above, the best fit for each single model to an absorber is judged ‘by-eye’ rather than using a statistical measure. Where multiple differing combinations are possible, we list both in our results. In order to decide a preference in these cases, we use the model parameters and their consistency with the galaxy observations (e.g. rotation velocities similar to the galaxy rotation are preferred), as well as comparable discs and outflows in the literature. The reasons for any such preference are discussed in the relevant part of Section 4 or Appendix B.

4 INDIVIDUAL SYSTEMS

Using the models described above, we can attempt to match the absorption observed in the multiple lines-of-sight around several galaxies. Whilst the models contain several free parameters, which will usually allow them to fit an individual component, the additional constraints from several sightlines enable us to determine the structures observed. Here we discuss some examples. We present galaxy and absorber properties, as well as illustrating the galaxy *HST* image, MUSE kinematics where available, and the location of the lines-of-sight. We then compare the observed absorption with that produced by our toy models. Other galaxy-absorber systems are included in Appendix B, with the combination of results from our subsample discussed in Section 5. The tables show all galaxies within 1 Mpc of at least one line-of-sight and all absorbers within 500 km s^{-1} of the main galaxy considered.

4.1 A-14

A-14 is a small galaxy with a mass $\sim 10^{8.5} M_\odot$ at redshift $z \approx 0.05$, with details given in Table 4 and illustrated in Fig. 3, yet with a

low redshift that makes it the largest galaxy in the field on the sky. The galaxy shows a clear velocity gradient in [O III] emission,² with strong absorption in sightline A at an impact parameter of ≈ 26 kpc. VPFIT has identified an additional weaker component bluewards of the galaxy in LOS-A, and there may be a component in LOS-B that is blended with higher-order Lyman transitions from $z \approx 0.399$, approximately 80 km s^{-1} redwards of the galaxy (the $n = 17 - 0$ and $n = 16 - 0$ Lyman transitions are visible at ≈ 0 and $\approx 150 \text{ km s}^{-1}$ from the systemic redshift of A-14). Note that the spectrum of LOS-C is blocked by a sub-DLA from redshift ≈ 0.56 , so no absorption can be detected.

Our toy models can simultaneously fit the strong absorption feature in LOS-A and contribute to the unexplained component of absorption in LOS-B, using a single outflow. The position angles of the two sightlines necessitate a wide opening angle, as shown in the schematic in Fig. 3. Both sightlines probe the edge of the conical outflow, so the geometry is not sensitive to the possibility of a hollow cone. An opening angle of $\approx 60^\circ$ and an outflow velocity of $\approx 70 \text{ km s}^{-1}$ are sufficient to produce the observed velocities and column densities of the two absorbers. Ideally we would consider the presence of metal lines for possible further evidence of warm, metal-enriched material. However, the low redshift of this galaxy means that our COS data lack coverage of several metal lines, such as O VI, that might indicate outflows.

VPFIT finds that a weak, broad component at a very similar wavelength improves the fit on the wings of this strong absorption feature. Its width would suggest a hot component, but an outflow could not produce this width whilst also approximating the stronger component and a power-law halo would produce absorption in B that is not observed. A ‘patchy’ halo, or one with an extremely steep density profile, may be a plausible explanation. This could also be a detection of the warm-hot intergalactic medium (WHIM).

There is also a weak absorption component identified in LOS-A at 220 km s^{-1} bluewards of the galaxy. This is only marginally above the uncertainty limit used to remove noise spikes masquerading as absorbers (described in T14). Although its velocity offset is in the same direction as the rotation of the galaxy ISM, it is far larger than the both detected rotation speed of the galaxy and its estimated virial velocity. We therefore consider it unlikely that this absorber originates from an extended gaseous disc around this galaxy, and its low column density and large velocity offset mean that it is doubtful

²Because of a strong sky line in close proximity to $\text{H}\alpha$ at this redshift, the fainter emission in the outer parts of the galaxy is vulnerable to being ‘shifted’ in wavelength by up to a few \AA during the sky subtraction process (see section 2 of Cantalupo et al. 2019). We therefore choose to present the [O III] emission from this galaxy, which is unaffected by sky lines.

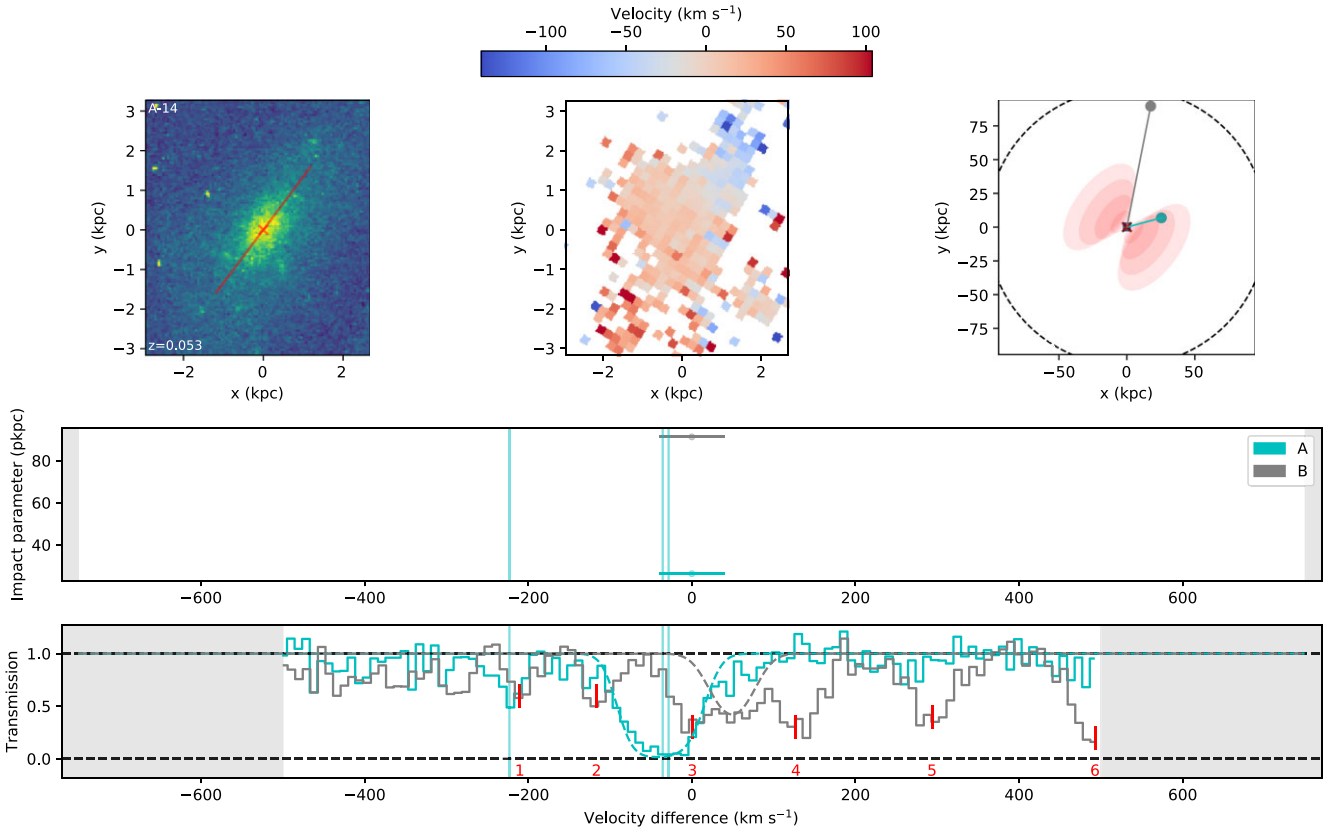


Figure 3. Details of the absorption and galaxy environment around MUSE galaxy A-14, using [O III] as observed in MUSE for the velocity map. Top left-hand panel: *HST* white-light image of the galaxy. The overlaid red line shows the projected major axis as found by GALFIT. Top-middle: Line-of-sight velocity obtained from fitting to the [O III] emission line as observed in MUSE. Top right-hand panel: A wider view of the geometry of the system on the sky, showing the lines joining the centre of the galaxy to each QSO (A in cyan, B in grey, C in orange). The black dashed circle indicates the virial radius of the galaxy, whilst the putative outflow is shown by the red ellipses. Additional crosses (where present) show the locations of other galaxies at this redshift. Central panel: The location of galaxies around this redshift, indicated as a function of impact parameter from the QSO sightlines and velocity difference from this galaxy (positive velocities showing galaxies redwards of this primary galaxy). The bolded galaxy features in the upper panels, whilst any other galaxies are faded. The horizontal bars show the velocity error arising from the galaxy redshift measurement. Each galaxy appears multiple times, once for each QSO, coloured as in the upper panels. Bottom panel: The transmission of the three QSO spectra at the wavelength of Ly α at the redshift of this galaxy, using the continuum fits described in Section 2.1 to normalize the spectra. The dashed horizontal lines show full and zero transmission. The solid vertical lines passing through both panels show the locations of Ly α absorption as found using VPFIT. The dashed lines coloured as in the other panels show the predicted absorption profiles given the preferred toy model described in the text (in this case an outflow with a velocity of ~ 70 km s $^{-1}$ and half-opening angle of $\sim 60^\circ$). Note that QSO-C (will be shown in orange throughout) is blocked by a sub-DLA at $z \approx 0.558$, so is excluded from this figure. Additional absorption features intervening from other redshifts are labelled by red tick marks and numbered from blue to red. In this case all six are Lyman lines from the same redshift as the sub-DLA, with features labelled 1 to 6 resulting from the $n = 19$ to $n = 14$ transitions.

whether this absorption is physically associated with this galaxy at all.

We can rule out a disc producing the strong absorption component in A, as this would generate absorption in B that is not consistent with the observations. Both sightlines probe the blueward portion of any model disc. If the rotating velocity component dominates, such a disc would produce absorption bluewards of the galaxy, where it would be detectable. If the infall velocity dominates, the absorption in B could be ‘hidden’ under the blended system, but the velocity required is much larger than both the free-fall and virial velocities, so we deem this unlikely.

Of the toy models we consider, a bi-conical outflow is therefore the most likely explanation for the strong absorber seen around this galaxy in the spectrum of QSO-A, although a disc with low HI column density is not ruled out and may contribute to a weaker absorption feature.

4.2 B-14

B-14 is also a low-luminosity galaxy ($\sim 0.05L_*$), although at a higher redshift of $z \approx 0.26$, inclined at $\approx 60^\circ$, illustrated in Fig. 4 and with details given in Table 5. Absorption is visible in all three sightlines, seen in the lower panel. The strongest component appears in LOS-B (column density $10^{14.8}$ cm $^{-2}$), at an impact parameter of ~ 100 kpc along the minor axis, with a velocity ~ 50 km s $^{-1}$ with respect to the galaxy. LOS-B exhibits O VI at the same velocity as this HI, as well as weak C III close to the galaxy redshift. The strongest HI component in LOS-A is 180 km s $^{-1}$ redshifted relative to the galaxy ($10^{14.2}$ cm $^{-2}$), although there appears to be a much weaker component ($10^{13.4}$ cm $^{-2}$) with a smaller velocity offset. This lies ~ 300 kpc away from the galaxy, and close to the major axis. No metals are detected in LOS-A, but the lower HI column density than in LOS-B means that the O VI to HI ratio of the gas in A could still be similar to that in B. The absorption in sightline C

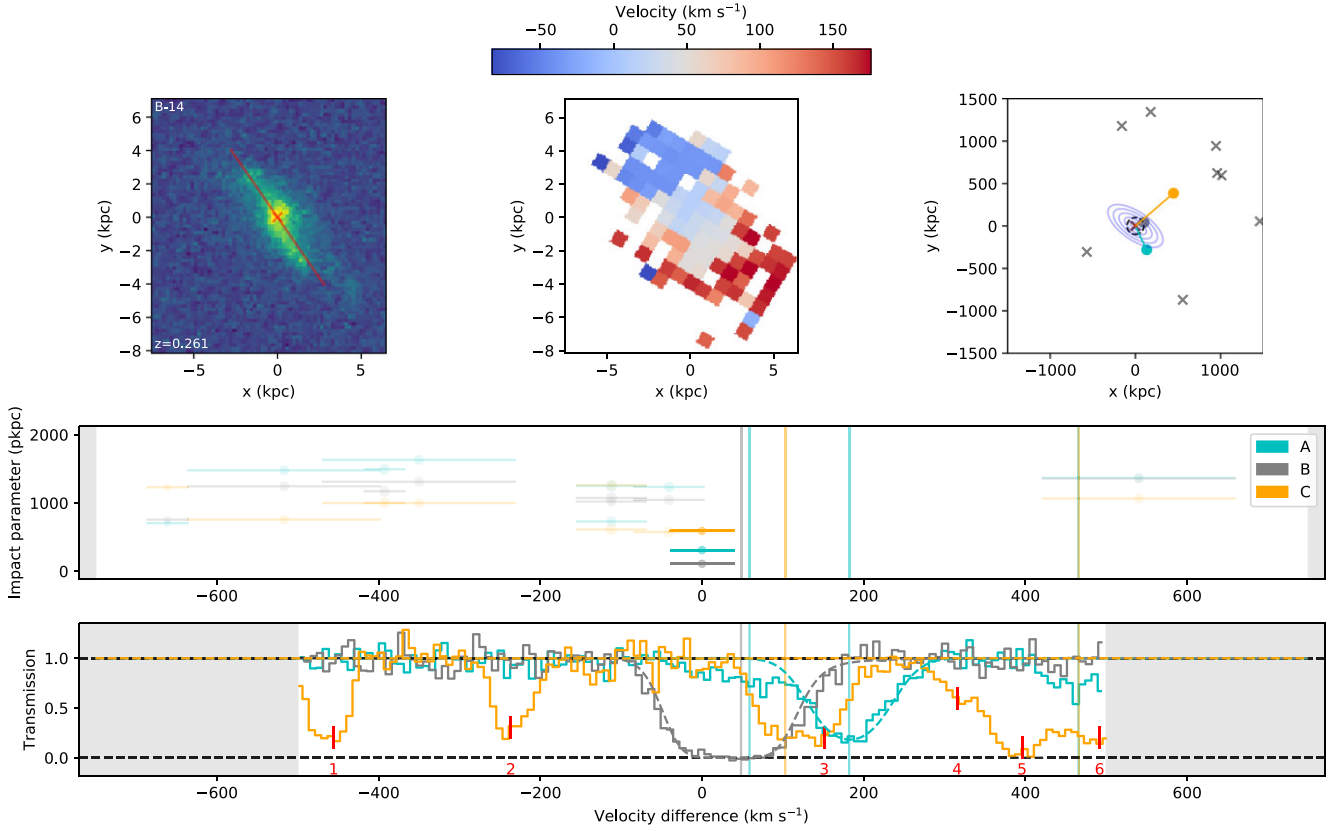


Figure 4. Details of the absorption and galaxy environment around MUSE galaxy B-14, a $\sim 0.05L_*$ galaxy at $z \approx 0.26$, using $H\alpha$ as observed in MUSE. The layout is identical to that shown in Fig. 3, with the model disc indicated by the blue ellipses. The model absorption is that produced by a disc with 270 km s^{-1} rotation velocity and 40 km s^{-1} infall velocity. Additional absorption features labelled are all identified as molecular H_2 lines from the sub-DLA at $z \approx 0.558$.

Table 5. Summary of galaxy–absorber group at $z \sim 0.261$. Additional galaxies and metal absorbers have velocities shown relative to the first galaxy (B-14). Column descriptions are given in Table 4.

Galaxy	z	Lum (L_*)	Inc	LOS	Imp (kpc)	Azimuth	$\log(N \text{ H I})$	b (km s^{-1})	Δv (km s^{-1})	Other ions
B-14	0.261	0.05	$64^\circ \pm 8^\circ$	A	310	$11^\circ \pm 13^\circ$	13.39 ± 0.05	44 ± 7	460 ± 60	–
	–	–	–	A	310	$11^\circ \pm 13^\circ$	14.15 ± 0.03	39 ± 2	180 ± 60	–
	–	–	–	A	310	$11^\circ \pm 13^\circ$	13.42 ± 0.09	67 ± 18	60 ± 60	–
	–	–	–	B	110	$76^\circ \pm 13^\circ$	14.82 ± 0.02	71 ± 4	50 ± 60	C III (0), O VI (+50)
	–	–	–	C	590	$85^\circ \pm 13^\circ$	13.85 ± 0.04	42 ± 6	470 ± 60	–
	–	–	–	C	590	$85^\circ \pm 13^\circ$	13.97 ± 0.03	34 ± 3	100 ± 60	–
(26595)	–	0.2	–	A	730	–	–	–	(–110)	–
	–	–	–	B	1022	–	–	–	–	–
	–	–	–	C	1262	–	–	–	–	–
(36043)	–	0.2	–	A	1235	–	–	–	(–40)	–
	–	–	–	B	1046	–	–	–	–	–
	–	–	–	C	575	–	–	–	–	–
(36413)	–	0.8	–	A	1249	–	–	–	(–110)	–
	–	–	–	B	1074	–	–	–	–	–
	–	–	–	C	611	–	–	–	–	–

has column density $10^{14.0} \text{ cm}^{-2}$, 100 km s^{-1} and 600 kpc away along the minor axis. Several other features in LOS-C are visible, but these are transitions from molecular hydrogen in the sub-DLA at $z \approx 0.56$.

The HI probed by LOS-A lies near the projected major axis, with a velocity offset in the same direction as the galaxy ISM emission, suggestive of co-rotating material. At first glance the absorption in

B could be an outflow, with a higher Doppler parameter and O VI detection possibly indicating heated material along the minor axis.

However, our toy models cannot reproduce the breadth and offset of the observed absorption without producing additional absorption in LOS-A or C that would be inconsistent with the observations. A disc model with both rotating and accreting velocity components can approximately reproduce the strongest absorption components

Table 6. Summary of galaxy–absorber group at $z \sim 0.728$. Any additional galaxies and metal absorbers have velocities shown relative to the first galaxy (31658). Note that this galaxy is beyond the redshift of QSO-C, so no absorption could be detected. Column descriptions are given in Table 4.

Galaxy	z	Lum (L_*)	Inc	LOS	Imp (kpc)	Azimuth	log(N H I)	b (km s $^{-1}$)	Δv (km s $^{-1}$)	Other ions
31658	0.728	0.40	$63^\circ \pm 4^\circ$	A	939	$66^\circ \pm 6^\circ$	14.20 ± 0.10	23 ± 4	-10 ± 40	–
–	–	–	–	A	939	$66^\circ \pm 6^\circ$	14.14 ± 0.10	36 ± 7	120 ± 40	–
–	–	–	–	B	608	$77^\circ \pm 6^\circ$	14.23 ± 0.01	134 ± 4	-60 ± 40	–

in both the A and B sightlines. The model shown in the lower panel of Fig. 4 uses velocities of 270 and 40 km s $^{-1}$, respectively, for these components. Although this absorber is broad (width ≈ 70 km s $^{-1}$), this is produced in our model with very little thermal/turbulent velocity, as the range of velocities probed as the line of sight passes through our model disc is sufficient. The required rotation velocity of ≈ 270 km s $^{-1}$ is substantially larger than both the observed galaxy rotation and the galaxy virial velocity (both $\lesssim 100$ km s $^{-1}$), so such rotation and accretion is difficult to physically motivate.

This model also leaves the absorption in C and the weaker component in A unexplained. The absorption in C has other galaxies at a similar distance (faded orange points in the central panel), some of which are substantially larger than B-14, so may not be associated with this galaxy. An outflow model with narrow opening angle $\lesssim 20^\circ$ could also explain this absorption in C without intersecting LOS-A or B, requiring an outflow velocity close to 150 km s $^{-1}$. The weak component at +60 km s $^{-1}$ in LOS-A is more likely to be associated with B-14, but still lies well beyond the virial radius. Any outflow wide enough to reach this line-of-sight would produce additional absorption in B, and is therefore ruled out. This absorption is broad, with a Doppler width ≈ 70 km s $^{-1}$, so may be probing the WHIM at temperatures $\approx 10^5$ K.

None of our toy models can reproduce all absorption components identified as Ly α within 500 km s $^{-1}$ of this galaxy. The disc model shown is the only model found to approximately match two of the four absorbers seen within 300 km s $^{-1}$ of the galaxy, and is compatible with the addition of a narrow outflow from LOS-C that would fit a third component of absorption.

An alternative model that can reproduce the strongest component in B is an outflow with $v_{\text{out}} \approx 100$ km s $^{-1}$ and $\theta_{\text{out}} \approx 45^\circ$. Such an outflow would produce additional absorption in C that is not observed. This better fits the expected parameter ranges than the rapidly rotating disc, as well as the metal content of absorption in B, but does not replicate either absorber seen in LOS-A and does not match that in C, so can only fit a single component.

Given the inconsistency between a strong outflow and the observations in LOS-C, we primarily consider the disc model in our later discussion.

4.3 31658

31658 is a $0.4 L_*$ star-forming galaxy at $z \sim 0.728$, detailed in Table 6 and Fig. 5. This is slightly beyond the redshift of QSO-C, so no absorption can be detected in this sightline. Ly α absorption is visible in both of the remaining lines-of-sight, which at this redshift lies in the lower resolution FOS spectra. The equivalent Ly β absorption does appear in COS, but this is blended with absorption features from multiple other redshifts, strongly affecting QSO-B. In A, the Ly β absorption is clearly made up of two components, as identified by VPFIT, but its low signal-to-noise makes it difficult to fit. As the Ly α absorption has higher signal-to-noise and does not appear to be affected by blending with absorption from other redshifts, we prefer to model the absorption in Ly α .

The position angles of absorption in both A and B are near the minor axis, but the similar azimuthal angles would probe the same cone of any outflow, so this cannot reproduce the velocity difference between the absorption in the two sightlines.

They would probe a putative disc at different azimuthal angles. A disc with a very large rotation velocity (>500 km s $^{-1}$) and comparatively small infall component (<30 km s $^{-1}$) would be required to reproduce the velocity difference between the absorbers, and still leaves one of the absorption components in A without explanation. It would also have to be extremely thin in order to produce strong absorption at A, with a larger impact parameter and nearer to the major axis. This is the model shown in Fig. 5. As the lines-of-sight would intersect such a disc at locations over 1 Mpc ($\approx 5r_{\text{vir}}$) from the galaxy, and the disc would have to be extremely thin and fast, it is unlikely to represent a physical structure in the IGM near this galaxy.

We therefore cannot produce a plausible model for the absorption around this galaxy using our simple disc and outflow models. Other possibilities include IGM absorption unassociated with a galaxy, and material associated with a galaxy that is fainter than the limit of our redshift survey.

All three absorbers have relatively large column densities for the IGM, above 10^{14} cm $^{-2}$. Our Paper 1 results suggest that the probability of finding a pair of such absorbers within 500 km s $^{-1}$ of a particular galaxy is ≈ 2 per cent, and therefore that these absorbers are likely associated with a galaxy.

Outside the MUSE fields, our detection limit at this redshift is $\approx 0.1 L_*$, whilst inside the MUSE fields detections are limited to a luminosity $\approx 0.06 L_*$ or a star-formation rate of $\approx 0.1 M_\odot \text{yr}^{-1}$. This allows for an undetected galaxy (or multiple galaxies) that could be producing some of these absorption components. Given the fairly high column densities at large impact parameters, this could plausibly explain at least some of the absorption in the A and B sightlines.

The combination of similar column densities, similar azimuthal angles, and a notable velocity offset, leads to the conclusion that simple disc, halo and outflow models are not likely explanations for the absorption around this galaxy.

5 DISCUSSION

In addition to the three example galaxies discussed above, a further nine isolated galaxies are described in Appendix B. More details on the models used are given in Appendix A. The best models found to fit each galaxy are summarized in Table 7.

We now discuss the results from our best-fitting models with regards to other studies using observational data and hydrodynamical simulations.

5.1 Outflows

Our toy model outflows can reproduce at least some of the absorption in four galaxies from our sample of 12, which are listed in Table 8. These include three small, star-forming galaxies, with outflows

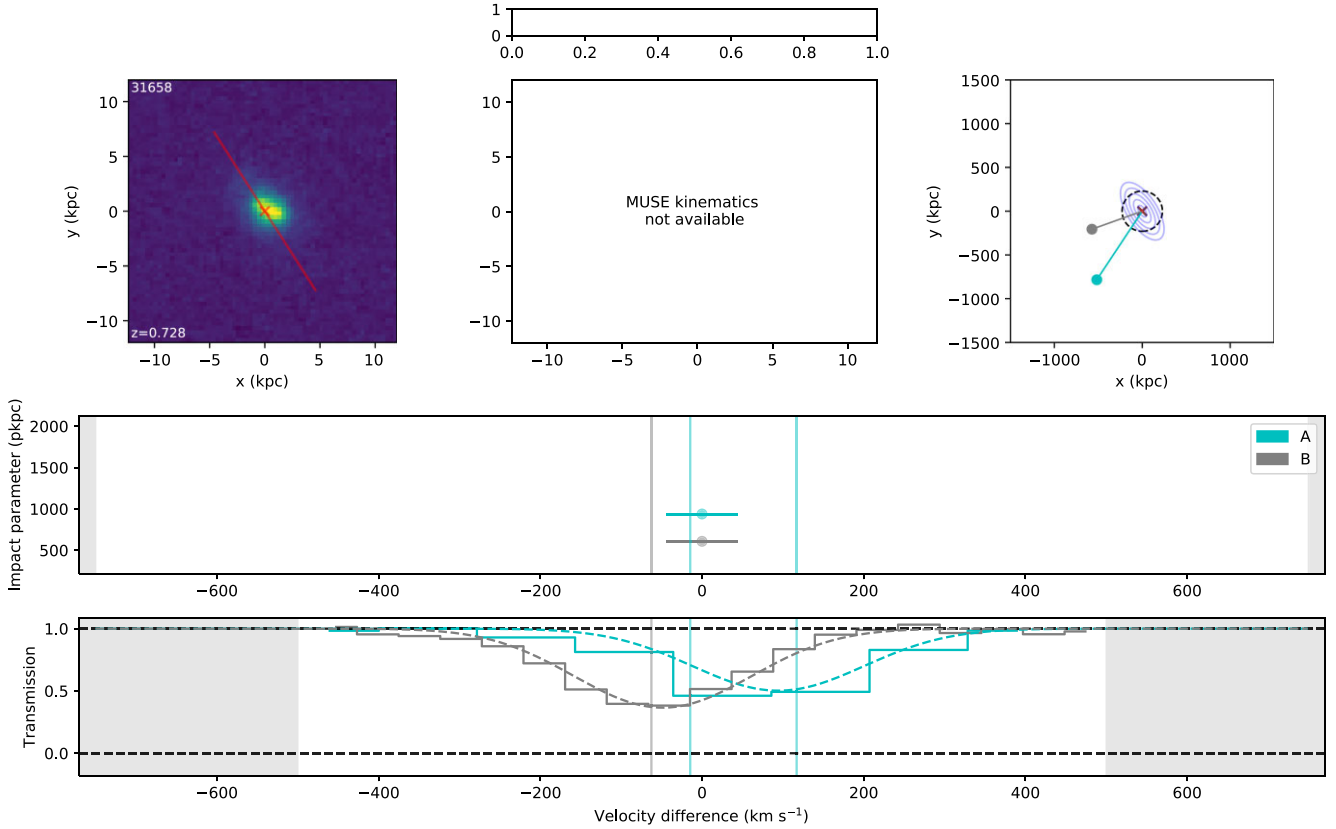


Figure 5. Details of the absorption and galaxy environment around galaxy 31658, a $\sim 0.4L_*$ galaxy at $z \sim 0.73$. The layout is identical to that shown in Fig. 3, and the model shown in the lower panel is disc with rotation velocity $\sim 550 \text{ km s}^{-1}$.

requiring a range of half-opening angles 20° – 60° , velocities of 70 – 150 km s^{-1} , and extents of $\lesssim 250 \text{ kpc}$. A-30 is a more massive, quiescent galaxy, which requires a much faster outflow with a much greater extent ($\sim 220 \text{ km s}^{-1}$ and $> 600 \text{ kpc}$). The $\approx 2.5 \text{ Gyr}$ required for the gas to travel this distance is sufficiently long that the galaxy’s apparent quiescence on short time-scales (based on lack of emission lines) does not rule out a stellar-feedback-driven outflow.

The extent of these outflows is comparable to the results from Paper 1, in which we showed a bimodality in the azimuthal angles of detected absorbers relative to galaxies extended to $\approx 300 \text{ kpc}$, and found evidence linking the major- and minor-axis absorbers with accretion and outflows. With one of the four putative outflows discussed here extending to approximately this distance, and another continuing substantially beyond that, the small sample from this work supports our conclusions from Paper 1.

Our outflow models are similar to those used in the MEGAFLOW survey (Schroetter et al. 2019), so we can compare our results directly. Both models allow for a hollow cone, but this is not necessary for any of the four galaxies for which outflows can match the observations. We also consider a constant velocity and r^{-2} density profile. However, their galaxy observations consist of a single MUSE field around each line-of-sight, limiting their impact parameters to generally $\lesssim 150 \text{ kpc}$, so we cannot judge the extent of their model outflows.

We use the same equation as in Veilleux, Cecil & Bland-Hawthorn (2005) (their section 4.6 and equation 4 from Schroetter et al. 2019) to estimate the escape velocities of outflows from our galaxies. Of these four galaxies, the two with the higher sSFRs have outflows exceeding escape velocity (A-62 and A-65 have $v_{\text{out}}/v_{\text{esc}}$ of ≈ 1.5 and

3, respectively), whilst those with lower sSFR do not (A-14 and A-30 have $v_{\text{out}}/v_{\text{esc}}$ of 0.9 and 0.8). This is also consistent with outflows escaping more frequently from lower-mass galaxies, as suggested by Schroetter et al. (2019). However, uncertainties on the model parameters are difficult to estimate, and those on the escape velocity are sufficiently large that these comparisons between the outflow and escape velocities are uncertain.

The model outflows from Schroetter et al. (2019) are also generally narrower than ours, with most half-opening angles $\approx 30^\circ$ or smaller. The opening angles from our models are constrained by the need to intersect or avoid intersecting each of the three lines-of-sight, so the narrower outflows they propose could not fit our observations of A-14 or A-30. We also note that three of our galaxies have lower masses than most included in the MEGAFLOW survey, which could be contributing to the wider outflows, as outflow collimation is expected to be a ‘path of least resistance’ effect (e.g. Tomisaka & Ikeuchi 1988; Nelson et al. 2019). Their geometric selection of likely outflows may also exclude outflows with wide opening angles.

There is disagreement between some of the largest numerical simulations on the extent of outflows, so our model results could in principle help to discriminate between the various feedback prescriptions included in these simulations. Although the strength of any conclusions drawn here is limited by a small sample, as well as model constraints motivated partially by simulations, it can still be useful to compare our models with outflows from simulations including EAGLE, Illustris, and FIRE.

Hopkins et al. (2021) find that the addition of cosmic rays to the FIRE-2 simulations allows some outflows from $\sim L_*$ galaxies to reach Mpc scales. The most massive galaxy that we find exhibiting

Table 7. Summary of isolated galaxies and the best-fitting toy models.

Galaxy	z	Figure	Table	Text	Best model(s)
A-14	0.053	3	4	4.1	(2/3 absorbers) Outflow, $\theta = 60^\circ$, $v = 70 \text{ km s}^{-1}$, extent $> 95 \text{ kpc}$ (Good fit, remaining component is weak with a large velocity offset)
26732	0.087	B1	B1	B1	(1/1 absorbers) Disc, height ratio ≈ 40 , $v_\phi = 550 \text{ km s}^{-1}$, $v_r = 120 \text{ km s}^{-1}$, extent $> 100 \text{ kpc}$ OR Outflow, $\theta = 50^\circ$, $v = 440 \text{ km s}^{-1}$, extent $> 100 \text{ kpc}$ (Only absorption component is weak with a large velocity offset)
25833	0.123	B2	B2	B2	(1/2 absorbers) Disc, height ratio ≈ 100 , $v_\phi = 700 \text{ km s}^{-1}$, $v_r = 20 \text{ km s}^{-1}$, extent $> 230 \text{ kpc}$ (Both absorption components have $\sim 500 \text{ km s}^{-1}$ velocity offset)
A-62	0.178	B3	B3	B3	(2/2 absorbers) Outflow, $\theta = 20^\circ$, $v = 150 \text{ km s}^{-1}$, extent 70–260 kpc (could have larger extent if constant rate/velocity assumptions relaxed)
A-65	0.220	B4	B4	B4	(2/2 absorbers) Outflow, $\theta = 30^\circ$, $v = 120 \text{ km s}^{-1}$, extent $> 260 \text{ kpc}$ AND Disc, height ratio ≈ 40 , $v_\phi = 220 \text{ km s}^{-1}$, $v_r = 50 \text{ km s}^{-1}$, extent $> 90 \text{ kpc}$
B-14	0.261	4	5	4.2	(2/4 absorbers) Disc, height ratio ≈ 10 , $v_\phi = 270 \text{ km s}^{-1}$, $v_r = 40 \text{ km s}^{-1}$, extent $> 330 \text{ kpc}$ (adjusting disc scale heights and adding spherical halo may help produce 3rd absorber)
A-63	0.488	B5	B5	B5	(1/3 absorbers) Outflow, $\theta = 20^\circ$, $v = 650 \text{ km s}^{-1}$, extent $> 350 \text{ kpc}$ (no good fit for this galaxy)
30169	0.584	B6	B6	B6	(no good fit for this galaxy)
31658	0.728	5	6	4.3	(2/3 absorbers) Disc, height ratio ≈ 300 , $v_\phi = 550 \text{ km s}^{-1}$, $v_r = 20 \text{ km s}^{-1}$, extent $> 1 \text{ Mpc}$
A-23	0.843	B7	B7	B7	(1/1 absorbers) Disc, height ratio ≈ 300 , $v_\phi = 350 \text{ km s}^{-1}$, $v_r = 30 \text{ km s}^{-1}$, extent $> 240 \text{ kpc}$ (possible weak component also fit if extent $> 550 \text{ kpc}$)
A-30	0.850	B8	B8	B8	(1/2 absorbers) Outflow, $\theta = 45^\circ$, $v = 250 \text{ km s}^{-1}$, extent $> 650 \text{ kpc}$ AND Disc, height ratio ≈ 40 , $v_\phi = 350\text{--}450 \text{ km s}^{-1}$, $v_r = 20\text{--}120 \text{ km s}^{-1}$, extent $> 40 \text{ kpc}$ (disc explains possible unidentified weak component) (remaining absorber is weak with a large velocity offset)
A-64	0.926	B9	B9	B9	(1/2 absorbers) Disc, height ratio ≈ 30 , $v_\phi = 150\text{--}350 \text{ km s}^{-1}$, $v_r = 0\text{--}200 \text{ km s}^{-1}$, extent $> 180 \text{ kpc}$

Table 8. Model outflow properties around galaxies for which outflows can reproduce some of the observed absorption components. Column descriptions: (1)–(5) are from Table 2; (6) specific star-formation rate; (7) maximum extent at which absorption is detected (at the point of highest H I density along the sightline with the largest impact parameter); (8) galaxy virial radius; (9) model half-opening angle; (10) model outflow velocity; (11) escape velocity from the location of the sightline at the maximum observed extent. Note that, as discussed in the text, the constant flow rate assumption could be relaxed slightly and allow for the outflow around A-62 to reach 260 kpc in extent.

Galaxy	z	M_\star $\log_{10}(M_\odot)$	M_h $\log_{10}(M_\odot)$	SFR $(M_\odot \text{ yr}^{-1})$	sSFR Gyr^{-1}	Extent (kpc)	r_{vir} (kpc)	θ_{out} ($^\circ$)	v_{out} (km s^{-1})	v_{esc} (km s^{-1})
(1)	(2)	(3)	(4)	(5)	(6)	(7)	(8)	(9)	(10)	(11)
A-14	0.053	8.7 ± 0.2	10.9 ± 0.3	$0.018^{+0.009}_{-0.006}$	$0.038^{+0.025}_{-0.015}$	95	90 ± 20	60	70	80 ± 20
A-62	0.178	8.7 ± 0.2	11.0 ± 0.3	$0.23^{+0.16}_{-0.09}$	$0.45^{+0.39}_{-0.21}$	70	90 ± 30	20	150	100 ± 30
A-65	0.220	7.6 ± 0.7	10.5 ± 0.7	$0.012^{+0.005}_{-0.003}$	$0.32^{+0.45}_{-0.30}$	260	70 ± 40	30	120	40 ± 20
A-30	0.850	10.7 ± 0.3	12.5 ± 0.7	$0.25^{+0.14}_{-0.09}$	$0.005^{+0.02}_{-0.004}$	650	290 ± 140	45	250	280 ± 140

a possible outflow does appear to reach at least 650 kpc, but the other three have much lower masses for which cosmic rays do not make a substantial difference (due to the relative reduction in cosmic ray pressure). Three additional galaxies in our sample with $M_\star > 10^{10} M_\odot$ do not produce absorption that is consistent with our model outflows, although the lines-of-sight do not probe their haloes near the projected minor axis. Such a small sample size means that we cannot determine whether large-scale outflows are common around such galaxies, and therefore whether cosmic rays are important to consider in discussions of the IGM.

Mitchell et al. (2020a) and Nelson et al. (2019) discuss outflows in EAGLE and TNG50 respectively. As expected, these works find that differences in the feedback prescriptions lead to different outflow characteristics. Mass flow rates in EAGLE remain approximately constant through concentric shells up to the virial radius of small galaxies in EAGLE, as is coded into our models, whilst mass flow

rate drops in TNG50. We therefore cannot use the detection of outflows at large impact parameters to favour EAGLE over TNG50. However, two of our proposed outflows could produce an improved fit if the flow rate (and velocity) were allowed to decrease with radius. This would favour the TNG model, but small sample size means that we cannot claim strong evidence of such a reduction in flow rate or velocity. Neither study considers outflows much beyond the virial radius in any detail, although Mitchell et al. (2020b) note that outflows from low-mass haloes must extend past the virial radius in order to explain metal enrichment in the IGM (e.g. Aguirre et al. 2001; Booth et al. 2012).

Both of these works include estimates of outflow velocity with galaxy mass in the inner CGM, generally producing outflows with velocities between 50 and 150 km s^{-1} for a wide range of halo masses, despite measuring outflows at different redshifts using different methods, although TNG50 outflows show a clearer increase in

outflow velocity with halo mass. Our model outflow velocities are not significantly different from the predictions of these simulations, despite much larger impact parameters.

Opening angles are also discussed in both simulation papers, but they use different measures that make it difficult to compare directly. Our small number of outflows have a wide range of opening angles, so it is not surprising that the measures adopted by Mitchell et al. (2020a) and Nelson et al. (2019) both produce estimates within this range ($\approx 50^\circ$ and $\approx 25^\circ$, respectively).

The parameters of our proposed outflows are therefore mostly compatible with the models from MEGAFLOW, as well as the EAGLE and FIRE simulations, with slightly more disagreement between our models and TNG50 (possibly related to their measurements being taken at higher redshifts).

5.2 Discs

Our toy model discs can also reproduce some of the absorption around five of our galaxies, namely A-65, B-14, 31658, A-23, and A-64. The required parameters of these discs are given in Table 9. The direction of rotation matches the stellar kinematics from MUSE for B-14 and A-64, whilst the MUSE data for A-23 does not exhibit a clear velocity gradient and no emission line fit was possible for A-65. Only the disc around B-14 is able to approximate multiple absorption components from the observations, whilst that around A-65 requires both an outflow and a disc in order to reproduce the data. The large extent and required velocity means that the absorption around galaxy 31658 is unlikely to represent a disc-like structure, so is not discussed further.

Our model discs are again similar to those used in MEGAFLOW, although tracing smaller column densities at larger impact parameters. In principle, the need to match absorption in the other lines-of-sight imposes constraints on the circular and infall components. The ratio of scale heights parallel and perpendicular to the disc are also constrained by the ratio of column densities at multiple azimuthal angles, or the need for absorption to remain weaker than our detection limit at certain azimuthal angles. The two scale heights and both components of velocity can therefore be treated as separate parameters that can be varied independently.

Unfortunately, most of the specific galaxies for which a model disc is compatible with the observations make only limited use of these constraints, as broad absorption in the other lines-of-sight can easily mask any absorption originating from our model disc, but cannot be fit by the disc (this applies to galaxies A-64, A-65, and 31658). The additional lines-of-sight therefore do not provide strong constraints on the disc parameters. B-14 is the only galaxy for which the absorption in multiple sightlines allows the rotating and infalling components to be determined separately.

We must therefore make assumptions on one component in order to determine the other. Purely circular orbits are not expected, especially at these large radii, and would require circular velocities larger than the virial velocity for all three model discs that are not well-constrained by multiple sightlines. Assuming free-fall for accreting material at large radii is incompatible with the constraints on A-23, and would still require velocities larger than virial for A-65.

Zabl et al. (2019) assume a value for $v_{\text{in}} = 0.6 v_{\text{vir}}$, motivated by results from Goerdt & Ceverino (2015). This is comparable to the best-fitting infall velocity for B-14, and requires circular velocities comparable to v_{vir} for A-23 and A-64. This is preferred by our model fits, despite requiring a circular velocity of $\approx 7 v_{\text{vir}}$ for A-65.

For the larger, higher redshift haloes A-23 and A-64, model discs with these assumed infall velocities and circular velocities $\lesssim v_{\text{vir}}$

can produce absorption that is consistent with the observations. For all assumed infall velocities on to A-65, and in order to fit the two strong absorption components around B-14, our model discs would require circular velocities $> 2 v_{\text{vir}}$. Such a large velocity is not likely to physically represent a disc-like structure, and suggest that the gas may instead be associated with a different galaxy.

Several previous works have used disc-like models to study the rotating component of the CGM. Ho & Martin (2019) use the shape of galaxy spiral arms for a small sample of sightlines probing the inner CGM of low- z galaxies, in order to constrain the direction of the galaxy inclination, and therefore the line-of-sight component of any infall velocity. They find maximum infall velocities of $30\text{--}40 \text{ km s}^{-1}$ for two of their five galaxy-quasar pairs, and ruling out infall for another pair. Steidel et al. (2002) also find that Mg II absorption kinematics in the inner CGM are likely dominated by rotation. Simple toy models underpredicted the co-rotation fractions seen in Ly α by French & Wakker (2020), but they used a tighter definition of co-rotation than our work by fitting a rotation curve to the galaxy spectrum. The rotating velocity component is substantially larger than the infall component for both of our galaxies with model discs probed at distances $\lesssim r_{\text{vir}}$, consistent with these previous results.

Rotating structures in the CGM are generally aligned with the central galaxy in most simulations, and this is supported by observations including our Paper 1. DeFelippis et al. (2020) find a ‘wedge’ of cool gas with angular momentum well-aligned with that of the galaxy, that extends to $\approx 1/2$ of the virial radius for small to medium-sized haloes in Illustris. Both EAGLE (Huscher et al. 2021) and FIRE-2 (Hafen et al. 2022) find that cool gas is rotationally supported around L_* galaxies only on small scales ($\approx 40 \text{ kpc}$). The results from our more massive haloes are at much larger impact parameters than this, and require a substantial infalling component if they are bound within the halo, so are not rotationally supported. Probes with smaller impact parameters (e.g. Tejos et al. 2021, although they find primarily pressure support) would be needed to detect the rotational support expected in the inner CGM.

Ho et al. (2020) discuss the rotation of Mg II structures in EAGLE, finding that a thick rotating structure is typical. Whilst the ratio of scale heights in our models is constrained by the column densities seen in multiple lines-of-sight, the scale heights themselves are partially degenerate with the central density, so are not well-determined. The vertical scale heights of $5\text{--}20 \text{ kpc}$ seen in Ho et al. (2020) and Steidel et al. (2002) can provide a reasonable fit for all four of our putative discs, but markedly different scale heights are also possible.

We only find two galaxies for which a rotating and/or accreting disc-like structure (with velocities $\lesssim v_{\text{vir}}$) can reproduce the observations, which therefore do not provide any substantial evidence for the extent or thickness of H I discs in the CGM.

5.3 Unattributed absorbers

There are also two galaxies around which all absorbing components have a large velocity offset ($> 300 \text{ km s}^{-1}$), and a further two for which our disc/outflow models cannot reproduce any of the absorbing components. In both cases for which all absorption is at a large velocity offset, only the A and B sightlines are available, and neither pass within the virial radius. 26732 is the lowest mass galaxy in the sample, whilst 25833 likely has the lowest sSFR (our given SFR estimate being an upper limit). It is therefore unsurprising that little absorption can be seen outside the virial radius of these galaxies.

The two galaxies for which our toy models could not reasonably match any of the absorption are A-63 and 30169. These both lie in the

Table 9. Model disc properties around galaxies for which discs can reproduce some of the observed absorption components. We include both velocity components under several assumptions of infall velocity. Where v_ϕ is left blank, this combination is not consistent with the observed absorption. Column descriptions: (1)–(4) are from Table 2; (5) model scale height ratio (i.e. relative disc thickness); (6) maximum observed disc extent (the 3-d distance from galaxy to the point on the line-of-sight where it intersects the disc plane, for the sightline with largest impact parameter with detected absorption); (7) virial radius; (8) virial velocity; (9) model circular velocity if infall assumed to be zero; (10), (12) model circular velocities if infall assumed to be $0.6 v_{\text{vir}}$ and the free-fall velocity at the maximum observed extent respectively; (11), (13) assumed infall velocities of $0.6 v_{\text{vir}}$ and the free-fall velocity at the maximum observed extent.

Galaxy	z	M_\star $\log_{10}(M_\odot)$	M_h $\log_{10}(M_\odot)$	h_r/h_z	Extent (kpc)	r_{vir} (kpc)	v_{vir} (km s^{-1})	$v_r = 0$	$v_r = 0.6 v_{\text{vir}}$	$v_r = v_f$		
								v_ϕ (km s^{-1})	v_ϕ (km s^{-1})	v_r (km s^{-1})	v_ϕ (km s^{-1})	v_r (km s^{-1})
A-65	0.220	7.6 ± 0.7	10.5 ± 0.7	40	90	70 ± 40	50 ± 30	400	360	30	360	35
B-14	0.261	8.5 ± 0.2	10.9 ± 0.3	10	330	90 ± 20	70 ± 20	–	270	41	270	47
31658	0.728	10.6 ± 0.2	12.4 ± 0.6	300	1070	220 ± 150	230 ± 150	530	–	137	–	200
A-23	0.843	10.7 ± 0.3	12.5 ± 0.7	300	240	230 ± 150	250 ± 160	300	270	151	–	330
A-64	0.926	10.4 ± 0.5	12.1 ± 0.8	30	180	160 ± 100	190 ± 120	340	160	113	20	280

redshift range for which all three sightlines are usable, and are close to edge-on and face-on respectively. For A-63, all three sightlines are close to the minor axis, so a disc is required to be extremely large with very high infall velocity in order to produce substantial line-of-sight velocities. Due to the high inclination, an outflow would also need a large velocity ($\approx 750 \text{ km s}^{-1}$) to match the absorption. For 30169, all three sightlines probe similar impact parameters, but have much larger differences in observed column density and velocity, which our models cannot reproduce.

As we note in Section 3, the reality of the gas flows is likely far more complex than our toy models can capture. However, for both of these galaxies it seems unlikely that over-simplification of our toy models is the cause of their failure to match observations. For example, it is difficult to conceive of a plausible outflow model in which lines-of-sight in opposite directions near the minor axis produce the similar velocity offsets seen near A-63.

Whilst both appear isolated, the detection limits allow for the presence of an unseen companion galaxy ($\lesssim 0.06 L_\star$ or $\lesssim 0.1 M_\odot \text{ yr}^{-1}$ SFR at 30169, $\lesssim 0.03 L_\star$ or $\lesssim 0.05 M_\odot \text{ yr}^{-1}$ SFR at A-63). A companion to the east of 30169 could plausibly explain the absorption in both A and B, with a larger impact parameter to C matching the lack of observed absorption. An unseen companion would also seem to be a likely cause for the absorption in QSO-C at the redshift of A-63, as the impact parameter to A-63 is more than 1 Mpc.

Tidal interactions between galaxies can more easily affect the outer regions of the CGM, so the lack of any visible distortion in the stars or the ISM kinematics does not rule out such interactions distorting the CGM and leading to the observations that cannot be fit by our models (e.g. Fossati et al. 2019a; Dutta et al. 2020).

5.4 Reliability of attributing absorbers

As we describe when discussing each galaxy (Section 4 and Appendix B), for most galaxies we can rule out at least some of our toy models through the relative column densities and velocities of absorption components, and thereby constrain the origins of the absorbing material. To summarize, for four of our twelve galaxies we can rule out a disc or an outflow from producing the strongest absorber because such a model would be incompatible with the other lines-of-sight. For a further four galaxies, the additional sightlines provide substantial constraints on the model parameters without ruling out either model entirely. In addition, for almost all galaxies our halo models are ruled out due to absorbers with substantially different velocities along the different lines-of-sight and/or column densities inconsistent with the expected reduction in density with

radius. Whilst single-sightline observations can use results from simulations and other observations to prefer one model over another (using properties such as metallicity and azimuthal angle), the additional lines-of-sight used here are clearly useful in constraining the possible models.

However, even with this additional information, it can be difficult to determine the robustness of the models we assign to the galaxies and absorbers. For example, how much to weight parameters in a range consistent with other literature, against a slightly improved fit (e.g. B-14 in our sample).

As noted throughout this work, these toy models are simplified, and do not take into account the changing ionization state of the gas, any ‘patchiness’ of the structures in the CGM, changes in velocities with distance (either for outflows or discs), or changes in the state of the CGM with time (such as an intermittent outflow, e.g. Muratov et al. 2017). Our toy models could therefore appear to rule out a disc or outflow in cases where the failure to fit the observations is due to one of these scenarios. We attempt to include these possibilities in our discussion of each individual galaxy.

Robustly identifying absorbers with outflowing or accreting material is a consistent challenge for transverse line-of-sight studies. Studies of this nature have used a cut in position angle and inclination in order to split absorbers into outflows and inflows, most often when studying Mg II at small impact parameters (Bordoloi et al. 2011; Schroetter et al. 2015, 2019; Zabl et al. 2019). We show the cut used by MEGAFLOW, alongside our sample of absorbers and whether we identify them as possible discs or outflows, in Fig. 6.

We find several absorbers that are best fit by a rotating structure at azimuthal angles close to the projected minor axis (similar to the single case found by Kacprzak et al. 2012a), and outflows relatively close to the major axis. Geometric cuts similar to those shown in the figure would therefore produce different identifications to the kinematic considerations we have included. This suggests that these cuts, whilst useful, are unlikely to be robust in determining whether an absorber is part of a disc or outflow.

Although disc-like absorption is found at all azimuthal angles, we do not see any evidence of outflowing H I within 25° of the major axis for these moderately inclined galaxies. This matches expectations for these structures and suggests that outflows at $z < 1$ do not fill a large majority of the solid angle.

Other observables that may aid in discriminating between infalling and outflowing material include column density (e.g. Kacprzak et al. 2019) and metallicity (e.g. Péroux et al. 2020). However, we find no substantial difference between the column densities of absorbers identified as discs and outflows by our toy models or those that

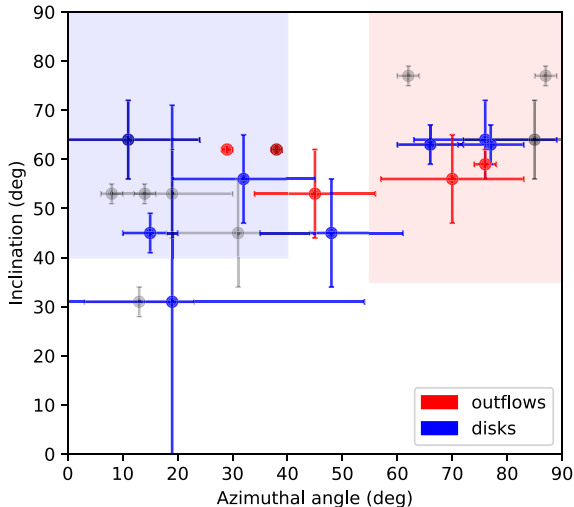


Figure 6. Azimuthal angle against inclination for galaxy-absorber pairs in our sample. Absorbers identified as probing a possible outflow are shown in red, with discs in blue and unattributed absorbers in grey. We also shade the regions used to identify the ‘primary’ disc and outflow subsamples in MEGAFLOW in blue and red, respectively (Schroetter et al. 2019; Zabl et al. 2019).

would be identified as such using geometric cuts. Some observations have failed to reproduce the expected metallicity difference between major- and minor-axis absorption (e.g. Kacprzak et al. 2019; Pointon et al. 2019), possibly due to contamination where high-metallicity and low-metallicity material cannot be distinguished along the line-of-sight. We also detect metals in too few of our absorbers for this to be useful. Neither column density nor metallicity can therefore be used reliably to identify absorbers originating from discs and outflows in these observations.

With only two or three sightlines passing each galaxy in our sample, in most cases each proposed model is only probed by a single line-of-sight, with a few models probed by two. This means that the model parameters are often not well-constrained, with degenerate effects on the resulting absorption. If a larger number of sightlines were available for each galaxy, these model structures could be probed by multiple sightlines, providing stronger constraints on the model parameters or ruling out a larger range of models. More complex models including physical processes such as entrainment and changes in velocity, temperature and ionization state would require even more information to constrain. However, even using only the two or three sightlines in this field we are often able to rule out many simple models, providing a clear improvement over single-sightline observations.

5.5 Broad absorbers

The CGM/IGM around our sample of galaxies appears to contain a substantial number of broad Ly α absorbers (BLAs), with Doppler widths above 40 km s⁻¹, expected to trace the warm-hot intergalactic medium (WHIM; e.g. Tepper-García et al. 2012; Pessa et al. 2018). Of the 27 absorbers identified as Ly α within 500 km s⁻¹ of our isolated galaxies, 19 have widths above 40 km s⁻¹, and 9 above 100 km s⁻¹. This is substantially larger than the 20–50 km s⁻¹ found to cover typical IGM absorbers (e.g. Davé et al. 2010).

However, the low resolution of the FOS spectra appears to be the main contributor to this abundance of BLAs. Many of our galaxies

and absorbers have redshifts above $z \approx 0.75$, such that both Ly α and Ly β are in the FOS spectra and cannot provide constraints on the line width, and several others are sufficiently weak that Ly β again fails to provide useful constraints on the Doppler width.

There are therefore only four BLAs near our isolated galaxies with $b > 50$ km s⁻¹ where the width is well-constrained by transitions appearing in the COS spectra (around A-14, A-62, and two near B-14, each discussed in the description of these galaxies), and five absorbers with widths of 40–50 km s⁻¹. Of the four candidate BLAs, two are fit by our models without a large thermal component. The range of line-of-sight velocities that would be produced by our toy models in these cases is sufficient to explain the width of the absorption. The other two cannot be fit by a disc/outflow model or our power-law haloes due to constraints from the multiple lines-of-sight, but may be produced by a more ‘patchy’ warm halo and/or the WHIM. The five 40–50 km s⁻¹ absorbers are all at a large velocity offset (> 350 km s⁻¹), and have impact parameters larger than the virial radius of the nearby isolated galaxy, and are therefore consistent with probing the IGM at temperatures of $\approx 10^{4.7}$ K (e.g. Tepper-García et al. 2012).

6 SUMMARY AND CONCLUSIONS

In this work, we model the absorption around twelve isolated galaxies in the Q0107 field in order to fit observations from the three lines-of-sight. This sample includes all galaxies with no detected companion within 500 kpc and 500 km s⁻¹, and covers both star-forming and passive galaxies with stellar masses $10^{7.5} \lesssim M_*(M_\odot) \lesssim 10^{10.5}$ across the redshift range $z < 1$. Motivated by results from Paper 1, as well as many other works, we focus in particular on whether co-rotating, disc-like structures and bi-conical outflows can reproduce the observed absorption. The use of three lines-of-sight provides additional constraints over previous works using QSO sightlines, although a small sample limits the strength of our conclusions.

We find that:

(i) Disc and outflow models can approximately reproduce ≈ 50 per cent of absorption features seen within 500 km s⁻¹ of isolated galaxies, rising slightly to ≈ 60 per cent of features within 300 km s⁻¹. However, the parameters required for these structures to match observations, such as large extents and velocities, are not always consistent with those expected based on results in the literature, possibly suggesting that the actual incidence of these physical structures is smaller.

(ii) Either a disc or outflow model can be ruled out as an origin of the strongest absorber within 300 km s⁻¹ of four of our twelve galaxies using the kinematics and column densities of absorption in the other lines-of-sight. The additional sightlines improve constraints on the model parameters around a further four galaxies. Multiple lines-of-sight therefore can be used to better determine the origins of absorption in the CGM/IGM.

(iii) Four of the twelve galaxies considered exhibit absorption consistent with a bi-conical outflow, which in three cases extend beyond the galaxy virial radius. Whilst only one of these produces clear absorption in multiple sightlines, the velocities found are consistent with the results from Schroetter et al. (2019), using Mg II to observe at smaller impact parameters. The two outflows around the galaxies with higher sSFR exceed escape velocity, whilst those with lower sSFR do not. We find two cases in which a substantial slowing or weakening of the outflow as it moves outwards can improve the fit over a constant-velocity outflow.

(iv) Five of the twelve galaxies exhibit absorption consistent with a rotating and infalling disc. Two of these fit the $\sim 0.6 v_{\text{vir}}$ infall velocity found by Goerdt & Ceverino (2015) and assumed by Zabl et al. (2019). The others are constrained to have a circular velocity larger than v_{vir} under most plausible assumptions of inflow velocity. These are therefore not likely to form physical disc-like structures, despite the disc model fit.

(v) Two of the galaxies feature no identified absorption within 350 km s^{-1} . These are the least massive galaxy and the least star-forming galaxy in our sample, consistent with expected dependencies on r/r_{vir} and sSFR.

(vi) Two of the galaxies do not have absorption that can be matched by a disc or outflow, despite lying near the star-forming main sequence. Whilst our toy models are oversimplified, this oversimplification is unlikely to be the reason for the failure of our models to reproduce the absorption around these two galaxies. These absorbers therefore have a different origin, possibly an undetected companion galaxy.

(vii) Only one galaxy requires both a disc and an outflow in order to reproduce the identified absorption components, although the existence of both structures is not ruled out for several others. We therefore cannot determine whether discs and outflows frequently exist simultaneously around the same galaxy, which could constrain the time-scales required for gas recycling.

(viii) At moderate inclinations of $\approx 40^\circ\text{--}70^\circ$, some absorbers best fit by disc-like structures can be found close to the projected minor axis (e.g. Kacprzak et al. 2012a; Tejos et al. 2021), and those best fit by outflows can be found down to 30° from the major axis. Geometric cuts using only azimuthal angle and inclination therefore do not appear sufficient to produce pure samples of disc and outflow absorbers.

The presence of multiple lines-of-sight near to individual galaxies clearly provides useful constraints on the structures in the CGM and IGM, providing estimates of outflow opening angles and velocities, and allowing rotating and in-falling velocity components of the expected accretion on to the galaxy to be separated. However, our study is limited by a small sample size. A larger sample would allow better exploration of the possible space of sightline configurations and galaxy properties. This would strengthen many of the tests we attempt here, as well as allowing us to determine how the model parameters vary with galaxy properties.

Constraining models of the structure of gas in the CGM/IGM is extremely difficult with single-sightline absorption measurements. Although the kinematics of material at high column densities in the inner CGM are becoming easier to observe using emission lines in wide-field IFUs (e.g. Finley et al. 2017; Burchett et al. 2021; Zabl et al. 2021; Leclercq et al. 2022), probing these structures at larger scales remains extremely challenging. Observing lower-column-density absorption in several locations around a single galaxy usually requires either a chance configuration of background QSOs or gravitationally lensed galaxies, or deep and time-consuming observations of background galaxies. Building a statistical sample of such models is therefore unlikely for some time, although several instruments due to be used on the ELT and other upcoming 30m-class telescopes include IGM/CGM tomography in their science cases (e.g. Maiolino et al. 2013; Evans et al. 2015; Marconi et al. 2021). This would allow a large sample of similar model results to be constructed at high redshifts.

In upcoming work we will apply similar procedures to galaxies that are clearly not isolated. This will add to our sample size, but will also include those for which the CGM is likely to be affected by interactions with other galaxies.

ACKNOWLEDGEMENTS

We thank the referee for their insightful comments that have improved the quality of this paper.

This work is based on observations made with the NASA/ESA *Hubble Space Telescope*, obtained from the data archive at the Space Telescope Science Institute. STScI is operated by the Association of Universities for Research in Astronomy, Inc. under NASA contract NAS 5-26555. We also make use of observations collected at the European Southern Observatory under ESO programmes 086.A-0970, 087.A-0857, and 094.A-0131; at the W.M. Keck Observatory under programme A290D; and at the Gemini Observatory under programme GS-2008B-Q-50.

We thank Matteo Fossati for providing the MARZ templates used for estimating redshifts and their uncertainties. We also thank Jill Bechtold for leading the effort to obtain the Keck data.

We thank the contributors to SCIPY,³ MATPLOTLIB,⁴ ASTROPY,⁵ and the PYTHON programming language, the free and open-source community and the NASA Astrophysics Data system⁶ for software and services.

This work also made use of the DiRAC system at Durham University, operated by the Institute for Computational Cosmology on behalf of the STFC DiRAC High Performance Computing (HPC) Facility.⁷

AB acknowledges the support of a UK Science and Technology Facilities Council (STFC) PhD studentship through grant ST/S505365/1. SLM acknowledges the support of STFC grant ST/T000244/1.

SC gratefully acknowledges support from Swiss National Science Foundation grants PP00P2_163824 and PP00P2_190092, and from the European Research Council (ERC) under the European Union's Horizon 2020 research and innovation programme grant agreement No 864361. MF also acknowledges funding from the ERC under the Horizon 2020 programme (grant agreement No 757535). This work has been supported by Fondazione Cariplo, grant No 2018-2329.

DATA AVAILABILITY

The raw data from the *Hubble Space Telescope* may be accessed from the MAST archive,⁸ and that from the WM Keck Observatory from the Keck Observatory Archive.⁹ That from the European Southern Observatory may be accessed from the ESO Archive,¹⁰ and that from the Gemini Observatory may be accessed from the Gemini Science Archive.¹¹ The relevant program IDs are given in Section 2 of this paper. The derived data generated in this research will be shared on reasonable request to the corresponding author.

³<http://www.scipy.org/>

⁴<https://matplotlib.org/>

⁵<https://www.astropy.org/>

⁶<https://ui.adsabs.harvard.edu/>

⁷<http://www.dirac.ac.uk/>

⁸<http://archive.stsci.edu/>

⁹<https://koa.ipac.caltech.edu/cgi-bin/KOA/nph-KOALogin>

¹⁰http://archive.eso.org/eso/eso_archive_main.html

¹¹<http://www.cadc-ccda.hia-ih.nrc-cnrc.gc.ca/en/gsa/>

REFERENCES

- Adelberger K. L., Shapley A. E., Steidel C. C., Pettini M., Erb D. K., Reddy N. A., 2005, *ApJ*, 629, 636
- Aguirre A., Hernquist L., Schaye J., Katz N., Weinberg D. H., Gardner J., 2001, *ApJ*, 561, 521
- Albaret F. D. et al., 2017, *ApJS*, 233, 25
- Anshul P., Narayanan A., Muzahid S., Beckett A., Morris S. L., 2021, *MNRAS*, 503, 3243
- Bacon R. et al., 2010, in McLean I. S., Ramsay S. K., Takami H., eds, Proc. SPIE Conf. Ser. Vol. 7735, Ground-based and Airborne Instrumentation for Astronomy III. SPIE, Bellingham, p. 773508
- Bahcall J. N., Spitzer L. Jr, 1969, *ApJ*, 156, L63
- Beckett A., Morris S. L., Fumagalli M., Bielby R., Tejos N., Schaye J., Jannuzi B., Cantalupo S., 2021, *MNRAS*, 506, 2574 (Paper 1)
- Behroozi P. S., Conroy C., Wechsler R. H., 2010, *ApJ*, 717, 379
- Bergeron J., 1986, *A&A*, 155, L8
- Bergeron J. et al., 1994, *ApJ*, 436, 33
- Bertin E., Arnouts S., 1996, *ApJS*, 117, 393
- Bielby R., Crighton N. H. M., Fumagalli M., Morris S. L., Stott J. P., Tejos N., Cantalupo S., 2017, *MNRAS*, 468, 1373
- Bielby R. M. et al., 2020, *MNRAS*, 493, 5336
- Bland J., Tully B., 1988, *Nature*, 334, 43
- Booth C. M., Schaye J., Delgado J. D., Dalla Vecchia C., 2012, *MNRAS*, 420, 1053
- Bordoloi R. et al., 2011, *ApJ*, 743, 10
- Bouché N., Hohensee W., Vargas R., Kacprzak G. G., Martin C. L., Cooke J., Churchill C. W., 2012, *MNRAS*, 426, 801
- Bouché N. et al., 2016, *ApJ*, 820, 121
- Bowen D. V., Chelouche D., Jenkins E. B., Tripp T. M., Pettini M., York D. G., Frye B. L., 2016, *ApJ*, 826, 50
- Brook C. B., Stinson G., Gibson B. K., Roškar R., Wadsley J., Quinn T., 2012, *MNRAS*, 419, 771
- Burchett J. N., Rubin K. H. R., Prochaska J. X., Coil A. L., Rickards Vaught R., Hennawi J. F., 2021, *ApJ*, 909, 151
- Cantalupo S. et al., 2019, *MNRAS*, 483, 5188
- Carswell R. F., Webb J. K., 2014, *Astrophysics Source Code Library*, record ascl:1408.015
- Charlton J. C., Churchill C. W., 1998, *ApJ*, 499, 181
- Chen H.-W. et al., 2020, *MNRAS*, 497, 498
- Concas A., Popesso P., Brusa M., Mainieri V., Thomas D., 2019, *A&A*, 622, A188
- Crighton N. H. M., Morris S. L., Bechtold J., Crain R. A., Jannuzi B. T., Shone A., Theuns T., 2010, *MNRAS*, 402, 1273
- D'Odorico V., Cristiani S., D'Odorico S., Fontana A., Giallongo E., Shaver P., 1998, *A&A*, 339, 678
- Davé R., Oppenheimer B. D., Katz N., Kollmeier J. A., Weinberg D. H., 2010, *MNRAS*, 408, 2051
- Davies R. L. et al., 1997, in Ardeberg A. L., ed., Proc. SPIE Conf. Ser. Vol. 2871, Optical Telescopes of Today and Tomorrow. SPIE, Bellingham, p. 1099
- DeFelippis D., Genel S., Bryan G. L., Fall S. M., 2017, *ApJ*, 841, 16
- DeFelippis D., Genel S., Bryan G. L., Nelson D., Pillepich A., Hernquist L., 2020, *ApJ*, 895, 17
- Dinshaw N., Weymann R. J., Impey C. D., Foltz C. B., Morris S. L., Ake T., 1997, *ApJ*, 491, 45
- Dutta R. et al., 2020, *MNRAS*, 499, 5022
- Dutta R. et al., 2021, *MNRAS*, 508, 4573
- Evans C. et al., 2015, preprint ([arXiv:1501.04726](https://arxiv.org/abs/1501.04726))
- Faber S. M. et al., 2003, in Iye M., Moorwood A. F. M., eds, Proc. SPIE Conf. Ser. Vol. 4841, Instrument Design and Performance for Optical/Infrared Ground-based Telescopes. SPIE, Bellingham, p. 1657
- Faucher-Giguère C.-A., Kereš D., Ma C.-P., 2011, *MNRAS*, 417, 2982
- Fielding D. B., Bryan G. L., 2022, *ApJ*, 924, 82
- Fielding D., Quataert E., McCourt M., Thompson T. A., 2017, *MNRAS*, 466, 3810
- Finley H. et al., 2017, *A&A*, 605, A118
- Finn C. W. et al., 2016, *MNRAS*, 460, 590
- Fossati M., Fumagalli M., Gavazzi G., Consolandi G., Boselli A., Yagi M., Sun M., Wilman D. J., 2019a, *MNRAS*, 484, 2212
- Fossati M. et al., 2019b, *MNRAS*, 490, 1451
- French D. M., Wakker B. P., 2020, *ApJ*, 897, 151
- Fumagalli M., Fossati M., Hau G. K. T., Gavazzi G., Bower R., Sun M., Boselli A., 2014, *MNRAS*, 445, 4335
- Fumagalli M., Cantalupo S., Dekel A., Morris S. L., O'Meara J. M., Prochaska J. X., Theuns T., 2016, *MNRAS*, 462, 1978
- Goerdt T., Ceverino D., 2015, *MNRAS*, 450, 3359
- Green J. C. et al., 2012, *ApJ*, 744, 60
- Hafen Z. et al., 2022, *MNRAS*, 514, 5056
- Heckman T. M., Armus L., Miley G. K., 1990, *ApJS*, 74, 833
- Hinton S. R., Davis T. M., Lidman C., Glazebrook K., Lewis G. F., 2016, *Astron. Comput.*, 15, 61
- Ho S. H., Martin C. L., 2019, *ApJ*, 888, 14
- Ho S. H., Martin C. L., Kacprzak G. G., Churchill C. W., 2017, *ApJ*, 835, 267
- Ho S. H., Martin C. L., Schaye J., 2020, *ApJ*, 904, 76
- Hopkins P. F., Chan T. K., Ji S., Hummels C., Keres D., Quataert E., Faucher-Giguère C.-A., 2021, *MNRAS*, 501, 3640
- Huscher E., Oppenheimer B. D., Lonardi A., Crain R. A., Richings A. J., Schaye J., 2021, *MNRAS*, 500, 1476
- Johnson S. D., Chen H.-W., Mulchaey J. S., 2015, *MNRAS*, 449, 3263
- Kaaret P. et al., 2020, *Nature*, 4, 1072
- Kacprzak G. G., Churchill C. W., Steidel C. C., Spitler L. R., Holtzman J. A., 2012a, *MNRAS*, 427, 3029
- Kacprzak G. G., Churchill C. W., Nielsen N. M., 2012b, *ApJ*, 760, L7
- Kacprzak G. G., Pointon S. K., Nielsen N. M., Churchill C. W., Muzahid S., Charlton J. C., 2019, *ApJ*, 886, 91
- Keeney B. A., Danforth C. W., Stocke J. T., France K., Green J. C., 2012, *PASP*, 124, 830
- Kennicutt J., 1998, *ARA&A*, 36, 189
- Kewley L. J., Geller M. J., Jansen R. A., 2004, *AJ*, 127, 2002
- Lan T.-W., Mo H., 2018, *ApJ*, 866, 36
- Le Fevre O., Crampton D., Felenbok P., Monnet G., 1994, *A&A*, 282, 325
- LeFevre O. et al., 2003, in Iye M., Moorwood A. F. M., eds, Proc. SPIE Conf. Ser. Vol. 4841, Instrument Design and Performance for Optical/Infrared Ground-based Telescopes. International Society for Optics and Photonics. SPIE, Bellingham, p. 1670
- Leclercq F. et al., 2022, *A&A*, 663, A11
- Lehnert M. D., Heckman T. M., Weaver K. A., 1999, *ApJ*, 523, 575
- Lehnert M. D., Le Tiran L., Nesvadba N. P. H., van Driel W., Boulanger F., Di Matteo P., 2013, *A&A*, 555, A72
- Lofthouse E. K. et al., 2020, *MNRAS*, 491, 2057
- Lopez S. et al., 2018, *Nature*, 554, 493
- Lopez S. et al., 2020, *MNRAS*, 491, 4442
- Maiolino R. et al., 2013, preprint ([arXiv:1310.3163](https://arxiv.org/abs/1310.3163))
- Maitra S., Srianand R., Petitjean P., Rahmani H., Gaikwad P., Choudhury T. R., Pichon C., 2019, *MNRAS*, 490, 3633
- Marconi A. et al., 2021, *The Messenger*, 182, 27
- Martin C. L., Ho S. H., Kacprzak G. G., Churchill C. W., 2019, *ApJ*, 878, 84
- Mathes N. L., Churchill C. W., Kacprzak G. G., Nielsen N. M., Trujillo-Gomez S., Charlton J., Muzahid S., 2014, *ApJ*, 792, 128
- Mitchell P. D., Schaye J., Bower R. G., Crain R. A., 2020a, *MNRAS*, 494, 3971
- Mitchell P. D., Schaye J., Bower R. G., 2020b, *MNRAS*, 497, 4495
- Montero-Dorta A. D., Prada F., 2009, *MNRAS*, 399, 1106
- Morris S. L., Jannuzi B. T., 2006, *MNRAS*, 367, 1261
- Morris S. L., van den Bergh S., 1994, *ApJ*, 427, 696
- Mortensen K., Keerthi Vasan G. C., Jones T., Faucher-Giguère C.-A., Sanders R. L., Ellis R. S., Leethochawalit N., Stark D. P., 2021, *ApJ*, 914, 92
- Muratov A. L. et al., 2017, *MNRAS*, 468, 4170
- Muzahid S., 2014, *ApJ*, 784, 5
- Muzahid S. et al., 2021, *MNRAS*, 508, 5612
- Nelson D. et al., 2019, *MNRAS*, 490, 3234
- Newman J. A. et al., 2013, *ApJS*, 208, 5
- Okoshi K. et al., 2021, *AJ*, 162, 175
- Pandya V. et al., 2021, *MNRAS*, 508, 2979

Peng C. Y., Ho L. C., Impey C. D., Rix H.-W., 2002, *AJ*, 124, 266
 Péroux C. et al., 2017, *MNRAS*, 464, 2053
 Péroux C. et al., 2019, *MNRAS*, 485, 1595
 Péroux C., Nelson D., van de Voort F., Pillepich A., Marinacci F., Vogelsberger M., Hernquist L., 2020, *MNRAS*, 499, 2462
 Pessa I. et al., 2018, *MNRAS*, 477, 2991
 Petry C. E., Impey C. D., Fenton J. L., Foltz C. B., 2006, *AJ*, 132, 2046
 Planck Collaboration VI, 2020, *A&A*, 641, A6
 Pointon S. K., Kacprzak G. G., Nielsen N. M., Muzahid S., Murphy M. T., Churchill C. W., Charlton J. C., 2019, *ApJ*, 883, 78
 Prochaska J. X., Weiner B., Chen H.-W., Mulchaey J., Cooksey K., 2011, *ApJ*, 740, 91
 Rubin K. H. R., Prochaska J. X., Koo D. C., Phillips A. C., 2012, *ApJL*, 747, L26
 Rubin K. H. R., Prochaska J. X., Koo D. C., Phillips A. C., Martin C. L., Winstrom L. O., 2014, *ApJ*, 794, 156
 Rubin K. H. R., Diamond-Stanic A. M., Coil A. L., Crighton N. H. M., Moustakas J., 2018, *ApJ*, 853, 95
 Ryon J. E., 2019, *Advanced Camera for Surveys HST Instrument Handbook*. Space Telescope Science Institute, Baltimore
 Salcido J., Bower R. G., Theuns T., 2020, *MNRAS*, 491, 5083
 Schroetter I., Bouché N., Péroux C., Murphy M. T., Contini T., Finley H., 2015, *ApJ*, 804, 83
 Schroetter I. et al., 2019, *MNRAS*, 490, 4368
 Scodreggio M. et al., 2005, *PASP*, 117, 1284
 Somerville R. S., Popping G., Trager S. C., 2015, *MNRAS*, 453, 4337
 Steidel C. C., Kollmeier J. A., Shapley A. E., Churchill C. W., Dickinson M., Pettini M., 2002, *ApJ*, 570, 526
 Stewart K. R. et al., 2017, *ApJ*, 843, 47
 Stocke J. T. et al., 2014, *ApJ*, 791, 128
 Swinbank A. M. et al., 2017, *MNRAS*, 467, 3140
 Tejos N. et al., 2014, *MNRAS*, 437, 2017 (T14)
 Tejos N. et al., 2021, *MNRAS*, 507, 663
 Tepper-García T., Richter P., Schaye J., Booth C. M., Dalla Vecchia C., Theuns T., 2012, *MNRAS*, 425, 1640
 Tomisaka K., Ikeuchi S., 1988, *ApJ*, 330, 695
 Tripp T. M., Sembach K. R., Bowen D. V., Savage B. D., Jenkins E. B., Lehner N., Richter P., 2008, *ApJS*, 177, 39
 Tumlinson J., Peebles M. S., Werk J. K., 2017, *ARA&A*, 55, 389
 Veilleux S., Cecil G., Bland-Hawthorn J., 2005, *ARA&A*, 43, 769
 Wang B., Heckman T. M., Zhu G., Norman C. A., 2020, *ApJ*, 894, 149
 Werk J. K., Prochaska J. X., Thom C., Tumlinson J., Tripp T. M., O'Meara J. M., Peebles M. S., 2013, *ApJS*, 204, 17
 Weymann R. J. et al., 1998, *ApJ*, 506, 1
 Wilde M. C. et al., 2021, *ApJ*, 912, 9
 Young P. A., Impey C. D., Foltz C. B., 2001, *ApJ*, 549, 76
 Zabl J. et al., 2019, *MNRAS*, 485, 1961
 Zabl J. et al., 2020, *MNRAS*, 492, 4576
 Zabl J. et al., 2021, *MNRAS*, 507, 4294
 Zahedy F. S., Chen H.-W., Rauch M., Wilson M. L., Zabludoff A., 2016, *MNRAS*, 458, 2423

APPENDIX A: MODEL DETAILS

To derive the angles and distances required to work with toy models of the gas distribution, we define axes relative to the galaxy, such that \hat{z} lies along the galaxy minor axis, with \hat{x} and \hat{y} along the major axis, such that \hat{x} is in the plane of the sky. If \hat{z} is defined to always have a northward component, \hat{x} and \hat{y} have westward and redward components, using the usual right-hand convention. (Note that these do not correspond to the x- and y-axis labels in the figures throughout this paper.)

We measure relative to the centre of the galaxy O , considering the point where the line-of-sight intersects the plane of the sky (B) and the points $A(D)$ a distance D along the LOS from B . $|\vec{OB}| = b$ for b

the observed impact parameter. Therefore

$$\vec{OB} = S_W b \cos(p) \hat{x} - S_N S_{Nr} b \sin(p) \cos(i) \hat{y} + S_N b \sin(p) \sin(i) \hat{z} \quad (A1)$$

As both position angle p and inclination i are recorded as between 0 and 90 degrees, sign terms are needed to differentiate the possible orientations. S_W and S_N are 1 if the LOS lies west of the galaxy minor axis and north of the major axis, respectively, and -1 otherwise (calculated from the coordinates of the galaxy and quasar). S_{Nr} is positive if the galaxy is inclined such that an outflow from the northern part of the galaxy would be travelling away from the observer. This is not constrained by the observations (although it is possible for one or two of our galaxies to constrain this through the direction of spiral arms, as in Ho & Martin 2019), but must be identical for different model structures around the same galaxy.

We then decompose the direction along the line of sight from B to A , a distance D along the LOS ($|\vec{BA}| = D$). Whether redward motion along the line of sight moves northward along the minor axis depends on the direction of the galaxies inclination:

$$\vec{BA} = D \sin(i) \hat{y} + S_{Nr} D \cos(i) \hat{z} \quad (A2)$$

This gives the total displacement from the centre of the galaxy to a point a distance D along the line of sight from the galaxy:

$$\vec{OA} = (S_W b \cos(p)) \hat{x} + (D \sin(i) - S_N S_{Nr} b \sin(p) \cos(i)) \hat{y} + (S_N b \sin(p) \sin(i) + S_{Nr} D \cos(i)) \hat{z} \quad (A3)$$

This is the relevant vector for determining the density at each point along the line-of-sight.

A1 Halo model

The halo model density as a function of position depends only on the distance from the galaxy centre. The displacement in equation (A3) correctly reduces to:

$$R = \sqrt{b^2 + D^2} \quad (A4)$$

We consider a power-law halo, with a density profile:

$$\rho = \rho_1 \left(\frac{R}{R_1} \right)^{-\alpha} \quad (A5)$$

There is no line-of-sight velocity component, except that introduced in thermal/turbulent velocity components and the instrumental line-spread-function. The reference density ρ_1 is defined at $R_1 = 1$ kpc. We also allow the halo to be offset from the galaxy redshift by a velocity v_δ , accounting for any redshift uncertainty or real peculiar velocity. The halo model therefore has four free parameters: v_t , v_δ , ρ_0 , and α .

A2 Outflow model

The outflow model has the same density profile as the isothermal halo ($\alpha = -2$) if the polar angle is within the cone defined by θ_{in} and θ_{out} . This maintains a constant flow rate with distance from the galaxy (equivalent to a constant rate of mass-loading from the galaxy). This constant flow rate is consistent with results from EAGLE (e.g. Mitchell et al. 2020a), but is not found in all simulations. We also do not consider any change in velocity due to gravitational or entrainment effects, or any change in the ionization state of the gas.

The projection of \vec{OA} in the galaxy plane is given by:

$$r = \sqrt{(b \cos(p))^2 + (D \sin(i) - S_N S_{Nr} b \sin(p) \cos(i))^2} \quad (A6)$$

and its projection along the galaxy minor axis is given by:

$$z = S_N b \sin(p) \sin(i) + S_{Nr} D \cos(i) \quad (\text{A7})$$

Note that z can be negative whilst r cannot.

The polar angle as a function of distance along the line-of-sight $\theta(D)$ is then given by $\tan(\theta) = r/z$.

For outflows, the bulk velocity of the gas is assumed to be entirely radial, so the velocity at the point A is along the vector \vec{OA} , and can easily be projected into the line of sight using $\vec{OA} \cdot \vec{BA}$.

The outflow model therefore has parameters v_r , ρ_1 , v_{out} , θ_{in} and θ_{out} , whilst S_{Nr} also affects the resulting model absorption.

A3 Disc model

For disc structures, we also define the azimuthal angle in the disc plane, such that $\tan(\phi) = y/x$ (with y and x the components of \vec{OA} in the disc plane). By construction, this means that ϕ is measured anticlockwise from $y=0$. This means that $v_y = \pm v_{circ} \cos(\phi)$ (the x component is perpendicular to the line-of-sight and the z -component is zero). This is positive if the line of sight is on the ‘red’ side of the galaxy minor axis, so can be stated as $v_y = S_W S_{Wr} v_{circ} \cos(\phi)$. We also allow a radial infall component within the plane of the disc, which must therefore have a y -component $v_y = -S_W v_r \sin(\phi)$. We add these components and project into the line-of-sight:

$$v_{LOS} = S_W \sin(i) (S_{Wr} v_\phi \cos(\phi) - v_r \sin(\phi)) \quad (\text{A8})$$

We note that setting $z = 0$, identifying the point at which the line-of-sight intersects the plane of the galaxy (and therefore the putative disc), reproduces the result given in Zabl et al. (2019) for their model thin discs:

$$R(z=0) = b \sqrt{1 + \sin^2(p) \tan^2(i)} \quad (\text{A9})$$

This value (for the line-of-sight with largest b in which absorption is detected) is the disc extent given for model discs throughout the main text. The effect of the ‘direction’ of the galaxy inclination (S_{Nr}) is included in the calculation of ϕ .

We use an exponential model for the density profile (as used for velocity models in e.g. Steidel et al. 2002), with scale heights h_r and h_z along the major and minor axes, respectively:

$$\rho = \rho_0 e^{\left(\frac{-r}{h_r}\right)} e^{\left(\frac{-|z|}{h_z}\right)} \quad (\text{A10})$$

This leaves our disc model with free parameters v_r , ρ_0 , v_ϕ , v_r , h_r , and h_z , one more than the outflow model. A disc may also have the additional degeneracy of the direction of rotation, if it is not determined by emission-line kinematics.

APPENDIX B: ADDITIONAL GALAXY MODELLING

We detail here the modelling and results from additional galaxies not included in the main paper.

B1 26732

Galaxy 26732 is a small ($0.01 L_*$) galaxy at $z \sim 0.087$. It is star-forming and lies ~ 1 Mpc away from a pair of larger galaxies. There is weak absorption in LOS-A substantially bluewards of the galaxy and slightly beyond the virial radius, and no detected absorption in B. (Note that C is not available due to the Lyman limit of a sub-DLA at $z \approx 0.56$.)

The large impact parameter makes it unlikely that the absorption in LOS-A originates from either of the larger galaxies. Both available lines-of-sight lie near the major axis, suggesting a disc as the more likely model. However, this would require a remarkably large rotational velocity for such a small galaxy, in the region of 550 km s^{-1} . (This can be varied by adding a substantial infall velocity component, but reducing the circular velocity to near the virial velocity would require a much faster infall than v_{vir} .) This galaxy lies outside the MUSE fields so galaxy kinematics are not available. Such a disc can approximately reproduce the absorption in A, without producing significant absorption in B.

Similarly, a wide, fast outflow with opening angle $\approx 50^\circ$ could also produce the absorption in A whilst remaining consistent with the noise in B, but the velocity required is close to 450 km s^{-1} . This is larger than all but one of the outflows proposed in Schroetter et al. (2019), and faster than the 90th-percentile velocities of outflowing gas in EAGLE outflows (Mitchell et al. 2020a). Given the weak absorption and large velocity offset, neither model is convincing and it seems more likely that this absorption is not physically associated with the galaxy. The line width of $\approx 50 \text{ km s}^{-1}$ is larger than most IGM absorbers. If primarily due to thermal velocities, this indicates gas hotter than most detected absorbing gas, suggesting that this could be a WHIM detection.

B2 25833

Galaxy 25833 is a small, non-star-forming galaxy at $z \approx 0.12$, at the same redshift as two smaller galaxies ~ 1 Mpc away. This is detailed in Table B2 and Fig. B2. The only visible absorption lies close to 500 km s^{-1} bluewards of the galaxy, and is relatively weak in both lines-of-sight. (The drop in transmission at $+500 \text{ km s}^{-1}$ is due to C III 977 Å from redshift $z \approx 0.4$.)

Position angles and inclinations for the other galaxies are not measured, so outflows and discs around these objects cannot be modelled. Despite a smaller impact parameter, the absorption in A is weaker than that in B. A is also marginally closer to the minor axis, so an outflow with a sufficiently wide opening angle to produce the absorption in B would produce stronger absorption in A, so this cannot reproduce the observations.

A disc also struggles to produce these absorber strengths, with an extremely thin disc required, as well as a rotation velocity that is not often found in such low-mass galaxies. The model shown in Fig. B2 is a disc with rotation velocity of 700 km s^{-1} and scale height ratio of 100:1. An outflow producing the absorption in A would also require a large velocity of $\approx 550 \text{ km s}^{-1}$. Therefore neither is a likely explanation for this absorption.

B3 A-62

A-62 is a star-forming galaxy, with details given in Table B3 and illustrated in Fig. B3. Absorption is seen in QSO-A but not in B, although there may be a weak Ly α feature in B that is not significant enough to be included in our line list. Their position angles are very similar on opposite sides of the galaxy, with A at much smaller impact parameter. Two components seen with similar column densities along the minor axis, along with O VI absorption, are consistent with a hollow-cone outflow. QSO-C is not available due to a saturated Lyman line from the sub-DLA, and the absorber at -400 km s^{-1} in LOS-A is a higher order Lyman line from a strong absorption system at $z \approx 0.54$.

Given the position angles and metal detection in the strong absorption feature in LOS-A, an outflow model would be preferred.

Table B1. Summary of galaxy–absorber group at $z \sim 0.087$. Any additional galaxies and metal absorbers have velocities shown relative to the first galaxy (26732). Note that this group is affected by the sub-DLA in the spectrum of QSO-C, so no absorption could be detected. Column descriptions are given in Table 4.

Galaxy	z	Lum (L_\star)	Inc	LOS	Imp (kpc)	Azimuth	$\log(N \text{ H I})$	b (km s^{-1})	Δv (km s^{-1})	Other ions
26732	0.087	0.01	$45^\circ \pm 4^\circ$	A	94	$15^\circ \pm 5^\circ$	13.47 ± 0.07	49 ± 11	-400 ± 100	–
	–	–	–	B	207	$13^\circ \pm 5^\circ$	(None, limit ≈ 13.2)	–	–	–
(37993)	–	0.4	–	A	1231	–	–	–	(+250)	–
	–	–	–	B	1112	–	–	–	–	–
(34203)	–	0.04	–	A	1282	–	–	–	(0)	–
	–	–	–	B	1212	–	–	–	–	–

Table B2. Summary of galaxy–absorber group at $z \sim 0.123$. Any additional galaxies and metal absorbers have velocities shown relative to the first galaxy (25833). Note that this group is affected by the sub-DLA in the spectrum of QSO-C, so no absorption could be detected. Column descriptions are given in Table 4.

Galaxy	z	Lum (L_\star)	Inc	LOS	Imp (kpc)	Azimuth	$\log(N \text{ H I})$	b (km s^{-1})	Δv (km s^{-1})	Other ions
25833	0.123	0.10	$53^\circ \pm 2^\circ$	A	238	$14^\circ \pm 2^\circ$	13.40 ± 0.06	48 ± 8	-490 ± 100	–
	–	–	–	B	372	$8^\circ \pm 2^\circ$	13.84 ± 0.03	45 ± 4	-470 ± 100	–
(17099)	–	0.04	–	A	890	–	–	–	(–340)	–
	–	–	–	B	1026	–	–	–	–	–
(34624)	–	0.04	–	A	1438	–	–	–	(+270)	–
	–	–	–	B	1490	–	–	–	–	–

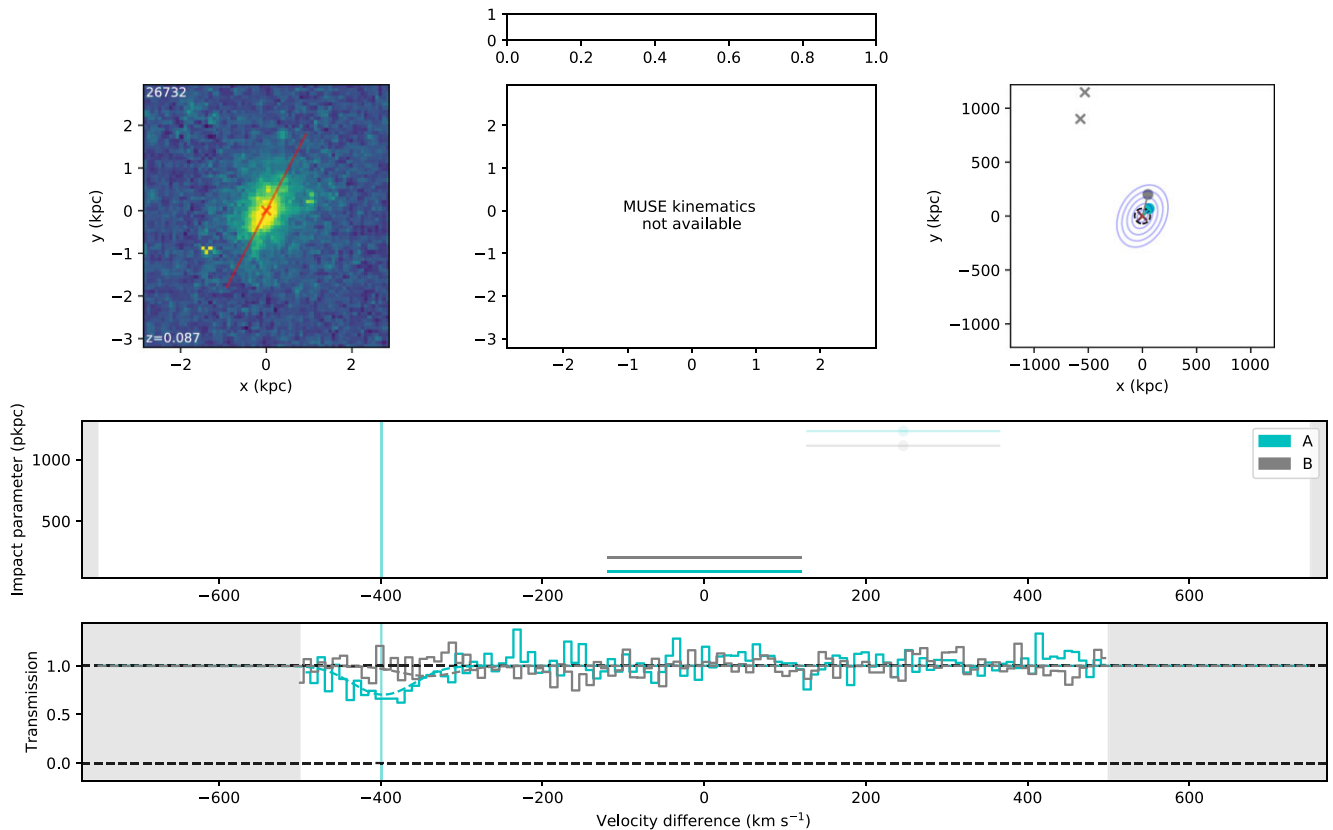


Figure B1. Details of the absorption and galaxy environment around galaxy 26732, a $\sim 0.01L_\star$ galaxy at $z \sim 0.09$. The layout is identical to that shown in Fig. 3, and the model shown in the lower panel is a disc with rotation velocity $\sim 550 \text{ km s}^{-1}$.

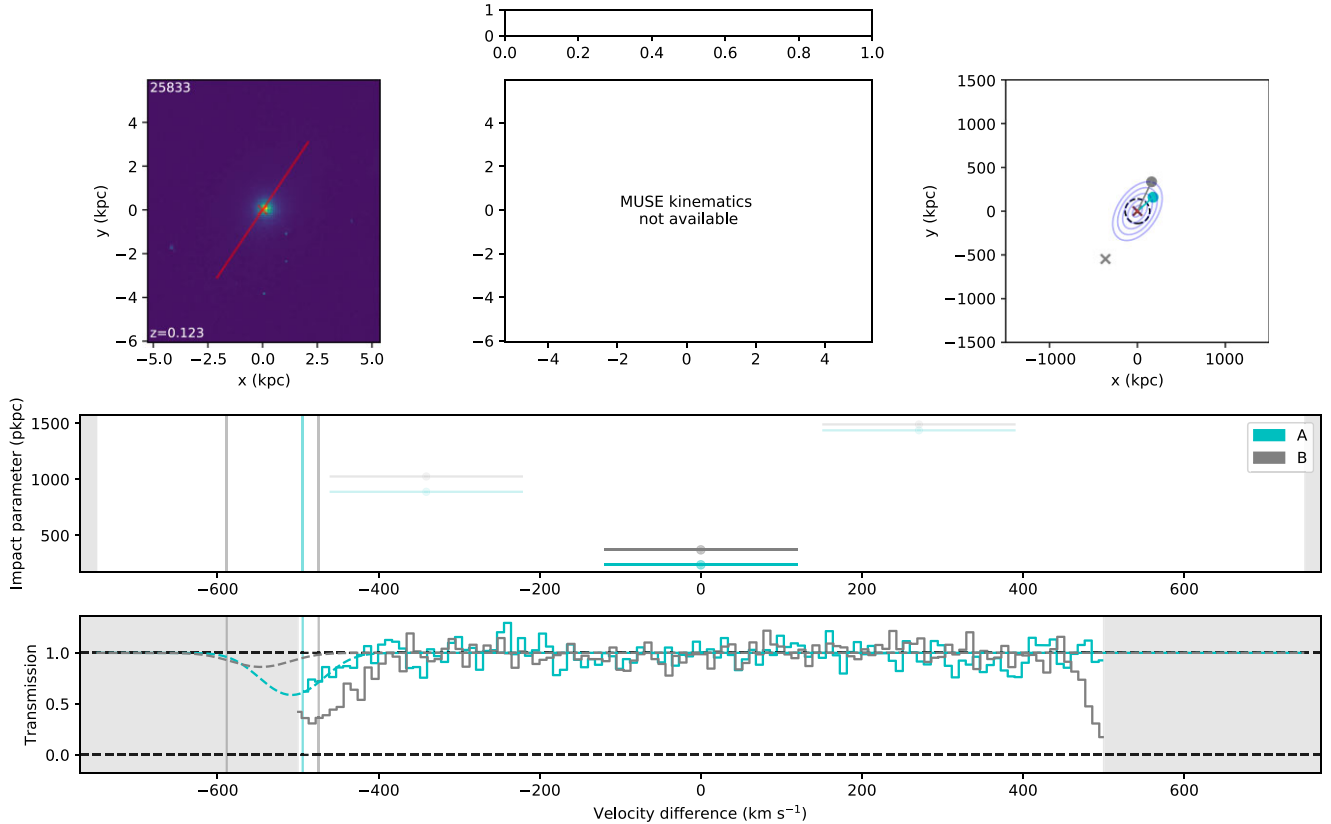


Figure B2. Details of the absorption and galaxy environment around galaxy 25833, a $\sim 0.1L_*$ galaxy at $z \sim 0.12$. The layout is identical to that shown in Fig. 3, and the model shown in the lower panel is a disc with rotation velocity $\sim 700 \text{ km s}^{-1}$.

Table B3. Summary of galaxy–absorber group at $z \approx 0.178$. Non-MUSE galaxies and metal absorbers have velocities shown relative to the first galaxy (A-62). Column descriptions are given in Table 4. Note that column density upper limits for non-detections are approximations in the absence of absorption from other redshifts.

Galaxy	z	Lum (L_*)	Inc	LOS	Imp (kpc)	Azimuth	$\log(N \text{ H I})$	b (km s^{-1})	Δv (km s^{-1})	Other ions
A-62	0.178	0.04	$59^\circ \pm 3^\circ$	A	45	$76^\circ \pm 2^\circ$	14.46 ± 0.03	57 ± 2	-70 ± 60	C III, O VI
–	–	–	–	A	45	$76^\circ \pm 2^\circ$	14.67 ± 0.04	9 ± 4	-40 ± 60	–
–	–	–	–	B	197	$80^\circ \pm 2^\circ$	(None, limit ≈ 12.9)	–	–	–
–	–	–	–	C	510	$47^\circ \pm 2^\circ$	(None, limit ≈ 13.0)	–	–	–

An outflow with a velocity of $\approx 150 \text{ km s}^{-1}$ and a half-opening angle of $\approx 30^\circ$ does approximately reproduce the absorption in LOS-A. However, in this case our models produce some absorption in LOS-B due to the constant velocity and constant flow rate conditions imposed. If this condition were relaxed, representing outflow material slowing due to a combination of gravity and interaction with the intergalactic medium, such an outflow may be consistent with the possible weak absorber seen near in LOS-B near the systemic redshift of the galaxy.

An alternative model could be material accelerating towards the galaxy along the line of sight, reaching $\approx 120 \text{ km s}^{-1}$ at the location of LOS-A. Due to the position angles close to the minor axis, any rotation of an extended disc cannot be determined. Emission lines from MUSE also lack any clear rotation. If this infall formed a disc-like structure, the physical distance would be substantially larger than that for an outflow, so an outflow is the preferred model.

We note that despite the line fitting procedure generating two absorption components in LOS-A, a hollow cone does not help to

improve the fit of the outflow model. The second component found in the fitting is substantially narrower than the COS line-spread-function and than most IGM absorbers (e.g. Davé et al. 2010), so may simply be a consequence of the changing physical distance (and therefore column density) along the line of sight. The stronger component is broad, and could be classified as a BLA, but this width is matched by the range of velocities produced by the outflow and does not require a large thermal component.

B4 A-65

A-65 is a small ($0.02 L_*$), star-forming galaxy at $z \approx 0.22$, with details in Table B4 and illustrated in Fig. B4. The A and B sightlines both feature absorption, with A lying close to the major axis and B close to the minor axis. The absorption in A is weaker and has a large velocity offset. The galaxy is faint so the signal-to-noise ratio of the emission lines is not sufficient to obtain coherent kinematics (from $H\alpha$ or O III). Note that the absorption seen at -400 km s^{-1} is Si III from a strong absorber at a slightly higher redshift of $z \approx 0.23$,

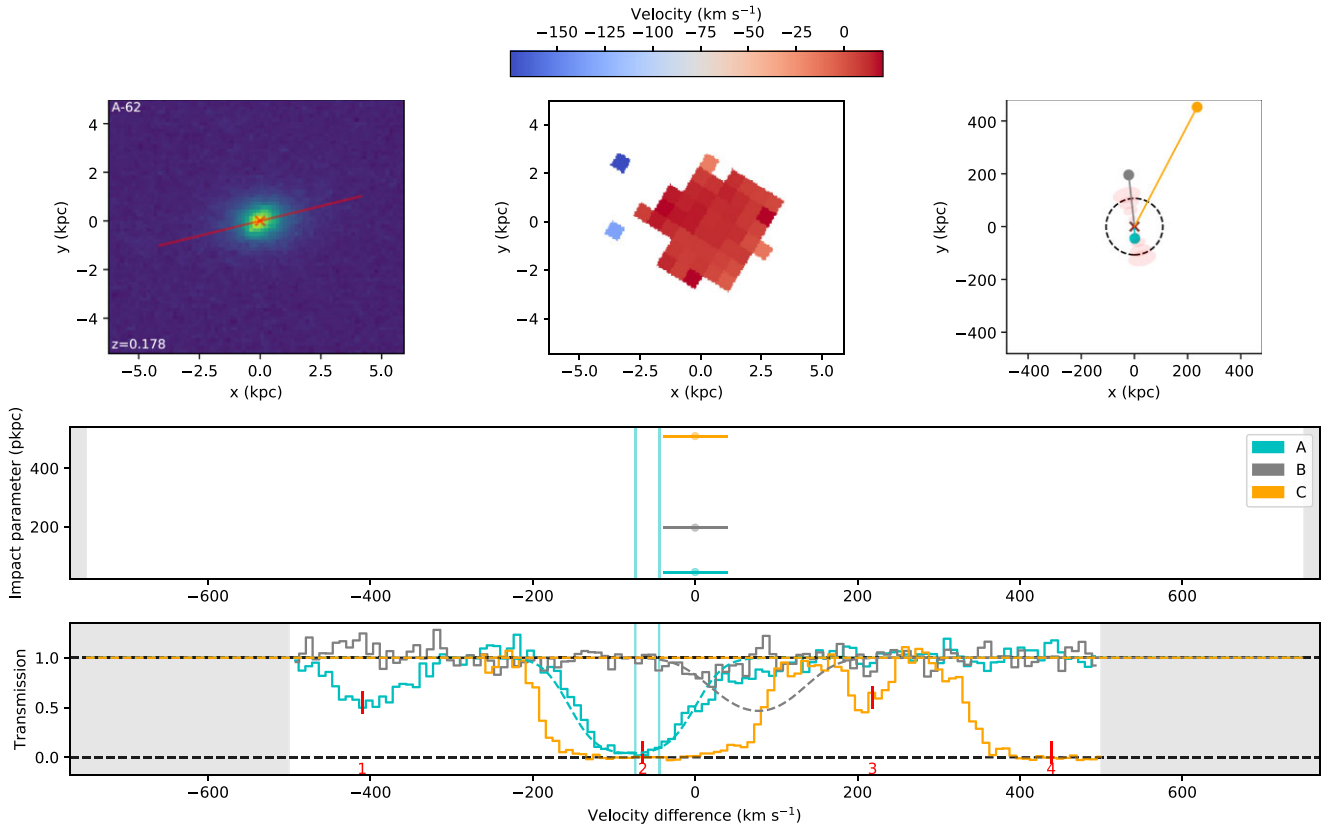


Figure B3. Details of the absorption and galaxy environment around galaxy A-62, using H α as observed in MUSE. The layout of the panels is identical to that in Fig. 3. The model shown is an outflow with a velocity of $\approx 150 \text{ km s}^{-1}$ and a half-opening angle of $\approx 30^\circ$. Additional absorption features that are not due to Ly α at this redshift are labelled with red tick marks as follows: (1) Lyman $n = 7$ from $z = 0.536$; (2) Lyman $n = 11$ from $z = 0.558$; (3) H2 molecular line from $z = 0.558$; (4) Lyman $n = 10$ from $z = 0.558$.

Table B4. Summary of galaxy–absorber group at $z \sim 0.220$. Non-MUSE galaxies and metal absorbers have velocities shown relative to the first galaxy (A-65). Column descriptions are given in Table 4.

Galaxy	z	Lum (L_*)	Inc	LOS	Imp (kpc)	Azimuth	$\log(N \text{ H I})$	b (km s^{-1})	Δv (km s^{-1})	Other ions
A-65	0.220	0.01	$56^\circ \pm 9^\circ$	A	73	$32^\circ \pm 13^\circ$	13.21 ± 0.05	33 ± 6	240 ± 40	–
–	–	–	–	B	262	$70^\circ \pm 13^\circ$	13.74 ± 0.04	35 ± 4	-70 ± 40	–
–	–	–	–	C	589	$69^\circ \pm 13^\circ$	(None, limit ≈ 12.9)	–	–	–

and the absorption feature visible in LOS-C at $\approx -120 \text{ km s}^{-1}$ is identified with Ly β at $z \approx 0.45$.

The position angles of absorption suggest that a model consisting of a disc and outflow could explain the two components. However, the near-identical position angles of B and C mean that any outflow producing the strongest absorption component in B would also produce absorption well above the detection limit in LOS-C, which is not observed. Any outflow wide enough and fast enough to produce the observed absorption in A will produce two absorption components in B that are clearly separated, unlike the observations.

Similarly, whilst an extended HI disc could be the origin of the absorption in A, requiring a rotation velocity of $200\text{--}400 \text{ km s}^{-1}$ (depending on any radial velocity component), the difference in impact parameter means that such a disc could not also cause the absorption seen in LOS-B.

We therefore cannot reproduce both observed absorption components using our simple disc/outflow models, without producing additional unobserved absorption. A model in which any cool clumps

in the putative outflow are heated in the IGM, or one in which the outflow velocity is insufficient to escape to larger scales, could explain the absorption observed in B yet lacking in C.

In conjunction with the extended disc fitting the absorption in A, a slowing or heating outflow could then reasonably match all observed absorption around this galaxy.

B5 A-63

A-63 is a $\sim 0.1L_*$ galaxy at $z \approx 0.488$, with details in Table B5 and illustrated in Fig. B5. It is isolated and highly inclined. A velocity gradient is visible in the MUSE data, but none of the three sightlines lie near the major axis.

The redshift is such that any associated Ly α lies in the FOS spectra, and therefore has much poorer spectral resolution than the COS spectra. Whilst VPFIT has identified absorption in sightlines B and C, it does not identify absorption in A, although the spectrum visible in the figure suggests possible weak, broad absorption. Ly β is visible at this redshift, but is too weak to provide a model fit.

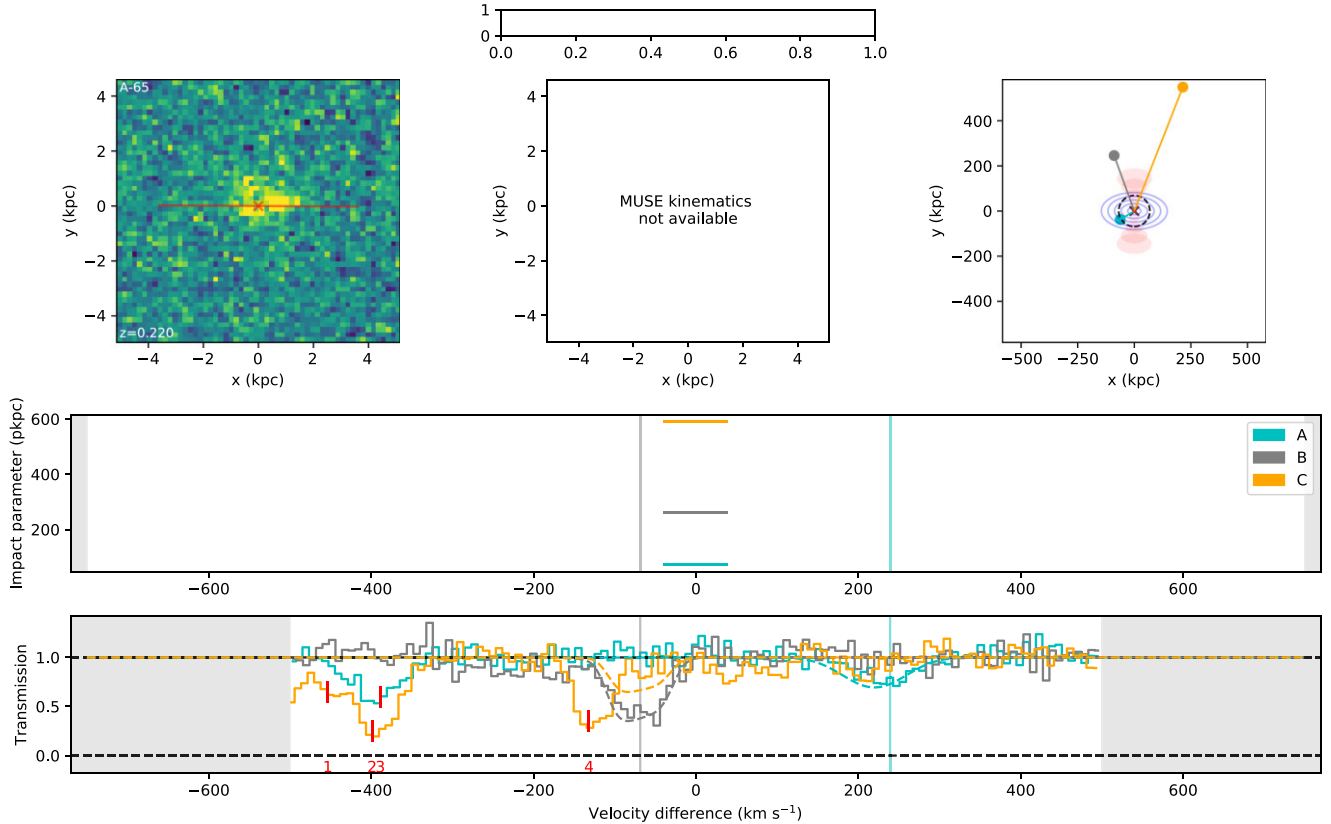


Figure B4. Details of the absorption and galaxy environment around galaxy A-65. The layout of the panels is identical to that in Fig. 3. The model shown combines a disc and an outflow. The putative outflow has a velocity of $\approx 120 \text{ km s}^{-1}$ and a half-opening angle of $\approx 30^\circ$, whilst the disc has a rotation velocity of 220 km s^{-1} and an infall velocity of 50 km s^{-1} . Absorbers originating from other redshifts are identified by the red ticks as follows: (1) Lyman $n = 6$ transition from $z = 0.579$; (2) and (3) Si III from $z = 0.227$; (4) Ly β from $z = 0.445$.

Table B5. Summary of galaxy–absorber group at $z \sim 0.488$. Any additional galaxies and metal absorbers have velocities shown relative to the first galaxy (A-63). Column descriptions are given in Table 4.

Galaxy	z	Lum (L_\star)	Inc	LOS	Imp (kpc)	Azimuth	$\log(N \text{ H I})$	b (km s^{-1})	Δv (km s^{-1})	Other ions
A-63	0.488	0.09	$77^\circ \pm 2^\circ$	A	144	$66^\circ \pm 2^\circ$	(None, limit ≈ 13.5)	–	–	–
–	–	–	–	B	345	$87^\circ \pm 2^\circ$	13.79 ± 0.05	230 ± 30	-190 ± 30	–
–	–	–	–	C	1003	$62^\circ \pm 2^\circ$	13.8 ± 0.2	260 ± 140	-80 ± 60	–
–	–	–	–	C	1003	$62^\circ \pm 2^\circ$	13.6 ± 0.2	130 ± 40	-430 ± 40	–

Both A and B lie close to the galaxy minor axis, but the absorption in both is blueward of the galaxy. An outflow therefore cannot explain both simultaneously. Similarly, no substantial component of the line-of-sight velocity offset to the absorber in B can come from rotation, and enough accretion to match that would produce a substantial redward component in A that is not observed.

An outflow can approximately match the absorption in B, but requires a very large outflow velocity of $\gtrsim 600 \text{ km s}^{-1}$ and a small opening angle of $\lesssim 20^\circ$ in order to produce the large velocity offset observed and avoid producing clear absorption in LOS-A. This is the model illustrated in Fig. B5. We note that this is much larger than typical stellar-feedback-driven outflows, which typically have velocities of $100\text{--}200 \text{ km s}^{-1}$ (e.g. Concas et al. 2019; Schroetter et al. 2019).

Our models cannot match the absorption in LOS-C in addition to the other sightlines, due to its much larger impact parameter yet similar column density.

The low column densities and large velocity offsets of the detected absorbers allow for the possibility that they are unassociated with the galaxy, and the lack of constraints on the absorber width allow for the possibility that these may be WHIM detections. The large velocities required to reproduce any of the absorption components do not support the existence of disc/outflow structures around this galaxy.

B6 30169

Galaxy 30169 is a near-face-on spiral galaxy outside of the MUSE fields (so no kinematics are available) at $z \approx 0.584$ (see Table B6 and Fig. B6). Absorption is visible in LOS-B, whilst features in A and B are identified with Lyman- β at $z \approx 0.88$, and no clear features are seen in the spectrum of QSO-C. Therefore only the blue wing visible in the absorber in LOS-B is likely Ly α . One other galaxy lies within 1 Mpc of QSO-C, but does not have a well-determined

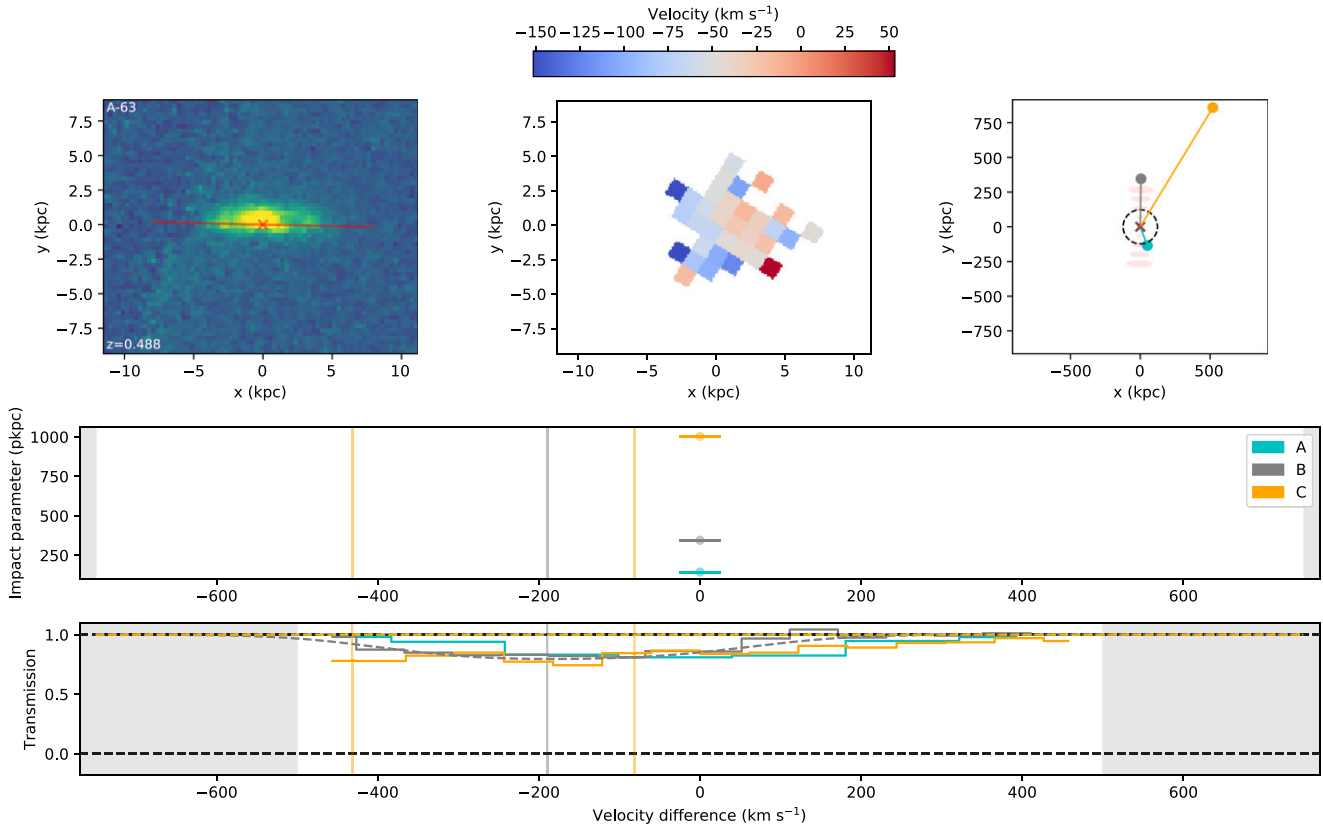


Figure B5. Details of the absorption and galaxy environment around galaxy A-63, a $\sim 0.09L_*$ galaxy at $z \sim 0.49$, using [O II] as observed in MUSE. The layout is identical to that shown in Fig. 3, and the model shown in the lower panel is an outflow with opening angle $\sim 20^\circ$ and velocity of 650 km s^{-1} .

Table B6. Summary of galaxy-absorber group at $z \sim 0.584$. Any additional galaxies and metal absorbers have velocities shown relative to the first galaxy (30169). Column descriptions are given in Table 4.

Galaxy	z	Lum (L_*)	Inc	LOS	Imp (kpc)	Azimuth	$\log(N \text{ H I})$	b (km s^{-1})	Δv (km s^{-1})	Other ions
30169	0.584	0.68	$31^\circ \pm 3^\circ$	A	672	$52^\circ \pm 10^\circ$	(None, limit ≈ 13.4)	–	–	–
	–	–	–	B	834	$13^\circ \pm 10^\circ$	13.67 ± 0.16	70 ± 30	-280 ± 30	–
	–	–	–	C	1002	$38^\circ \pm 10^\circ$	(None, limit ≈ 13.5)	–	–	–
(35758)	–	0.2	–	A	2035	–	–	–	(0)	–
	–	–	–	B	1673	–	–	–	–	–
	–	–	–	C	879	–	–	–	–	–

position angle and no other galaxies are within 500 km s^{-1} and 2 Mpc of the sightlines.

As the galaxy is close to face-on, a disc model cannot produce the large velocity offset to the absorber in LOS-B, without an extremely large velocity ($> 600 \text{ km s}^{-1}$). A conical outflow would be capable of generating such an offset, but would also produce absorption in the other two sightlines (as their impact parameters differ by less than a factor of two and position angle has only a weak effect at this inclination). An example of this is shown in the lower panel of Fig. B6.

Therefore neither the disc nor outflow model can reproduce the absorption component seen near this galaxy in LOS-B.

B7 A-23

A-23 lies at a redshift of $z \approx 0.843$, and is detailed in Table B7 and Fig. B7. The small apparent size of this galaxy makes it difficult to

obtain any kinematic gradient, and the uncertainty in position angle is large.

Absorption is detected in LOS-B with a substantial blueshift in comparison to the galaxy. There is also a possible weak feature in LOS-A, although this was not identified by VPFIT as it lies marginally below the significance threshold.

If the possible absorber in A is included, an outflow cannot simultaneously fit both absorbers, as they lie in opposite sides of the major axis (and hence probe opposing outflow cones) yet have the same direction of velocity offset.

A thin disc requires a large rotation velocity ($\sim 350 \text{ km s}^{-1}$) in order to match the velocity offset to the absorber in LOS-B. Due to B lying closer to the major axis, a thinner disc increases the column density of B in comparison to A and can produce a similarly strong absorber despite its larger impact parameter. The infall velocity is also constrained by the apparent absorption in LOS-

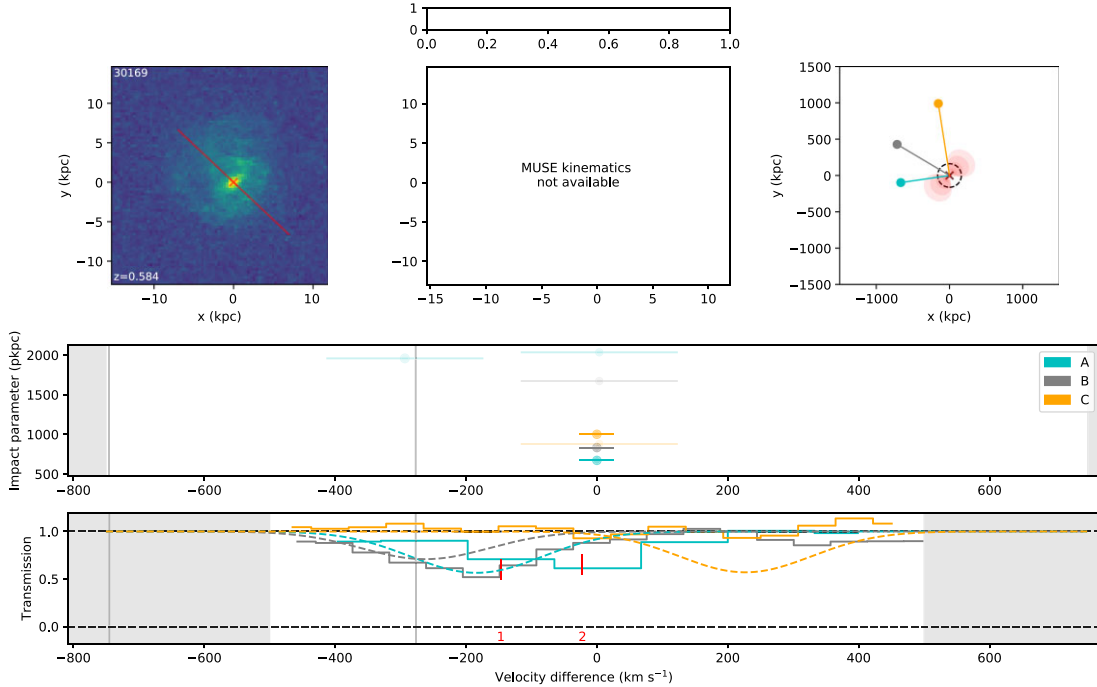


Figure B6. Details of the absorption and galaxy environment around galaxy 30169, a $\sim 0.7L_*$ galaxy at $z \sim 0.58$, using [O II] as observed in MUSE. The layout is identical to that shown in Fig. 3, and the model shown in the lower panel is an outflow with velocity $\sim 280 \text{ km s}^{-1}$ and opening angle 40° . Absorption originating from another redshift is marked by red ticks, with both components here identified as Ly β originating from $z = 0.876$.

Table B7. Summary of galaxy-absorber group at $z \sim 0.843$. Any additional galaxies and metal absorbers have velocities shown relative to the first galaxy (A-23). Note that this galaxy is beyond the redshift of QSO-C, so no absorption could be detected. Column descriptions are given in Table 4.

Galaxy	z	Lum (L_*)	Inc	LOS	Imp (kpc)	Azimuth	$\log(\text{N H I})$	b (km s^{-1})	Δv (km s^{-1})	Other ions
A-23	0.843	0.2 ± 0.02	$31^\circ \pm 40^\circ$	A	233	$68^\circ \pm 35^\circ$	(None, limit ≈ 13.5)	–	–	–
–	–	–	–	B	578	$19^\circ \pm 35^\circ$	13.61 ± 0.08	130 ± 30	-140 ± 40	–

A, as both sightlines have a similar line-of-sight velocity component from disc rotation, but opposite line-of-sight components from infall.

B8 A-30

A-30 lies at $z \sim 0.85$, and is detailed in Fig. B8 and Table B8. It is a non-star-forming galaxy, so lacks the emission lines necessary to produce kinematics. Strong absorption features in the spectrum are sufficient to provide a well-constrained redshift measurement.

Weak absorption is visible in LOS-B at $\approx 200 \text{ km s}^{-1}$ redwards of the galaxy, with a potential weak absorber at $\approx 400 \text{ km s}^{-1}$ in LOS-A. Additional absorption identified as Ly α is visible in both sightlines around 500 km s^{-1} bluewards of the galaxy. No other galaxy comes within 1.5 Mpc of any of the QSOs within 750 km s^{-1} of this galaxy. The absorbers lie in the low-resolution FOS spectra, but are too weak for Ly β to provide a better fit.

Due to its much smaller impact parameter, any disc cannot match the absorption in B without producing much stronger absorption in A, but a sufficiently narrow outflow can cause absorption in B without producing absorption in LOS-A. A half-opening angle of $\sim 45^\circ$ and an outflow velocity of $\sim 250 \text{ km s}^{-1}$ can reproduce the observed absorption.

If the possible weak absorber in A is real, then a disc can produce a reasonable fit, but the required velocities are quite large. The small

impact parameter means that a disc fitting the absorption in A will not produce any detectable absorption in B, making the rotating and infalling velocities degenerate. The rotation velocity can vary between $\sim 350 \text{ km s}^{-1}$ (if $0.6 v_{\text{vir}}$ infall) and $\sim 450 \text{ km s}^{-1}$ (if no infall), or could be made smaller with larger infall velocities.

The absorption at -400 km s^{-1} may be due to another galaxy outside the 750 km s^{-1} window shown.

B9 A-64

A-64 is another $\sim 0.1L_*$, isolated, star-forming galaxy. Some kinematics are available, showing a clear velocity gradient across the galaxy, although the signal-to-noise ratio is poor. This is detailed in Table B9 and illustrated in Fig. B9.

Similar absorbers are seen in the A and B sightlines, with comparable strengths and velocity offsets, neither lying close to the major or minor axis of the galaxy. As LOS-A lies at a smaller impact parameter and closer to the galaxy minor axis than LOS-B, an outflow cannot reproduce two absorbers with similar densities.

Any rotation in a putative disc would generate a substantial line-of-sight velocity difference between the absorption in the two sightlines, which is not observed. Additionally, a disc would have to be extremely thin ($\sim 1000:1$) for the position angle difference (B nearer the major axis) to counter the impact parameter difference (A nearer the galaxy) and produce similar-strength absorbers. A

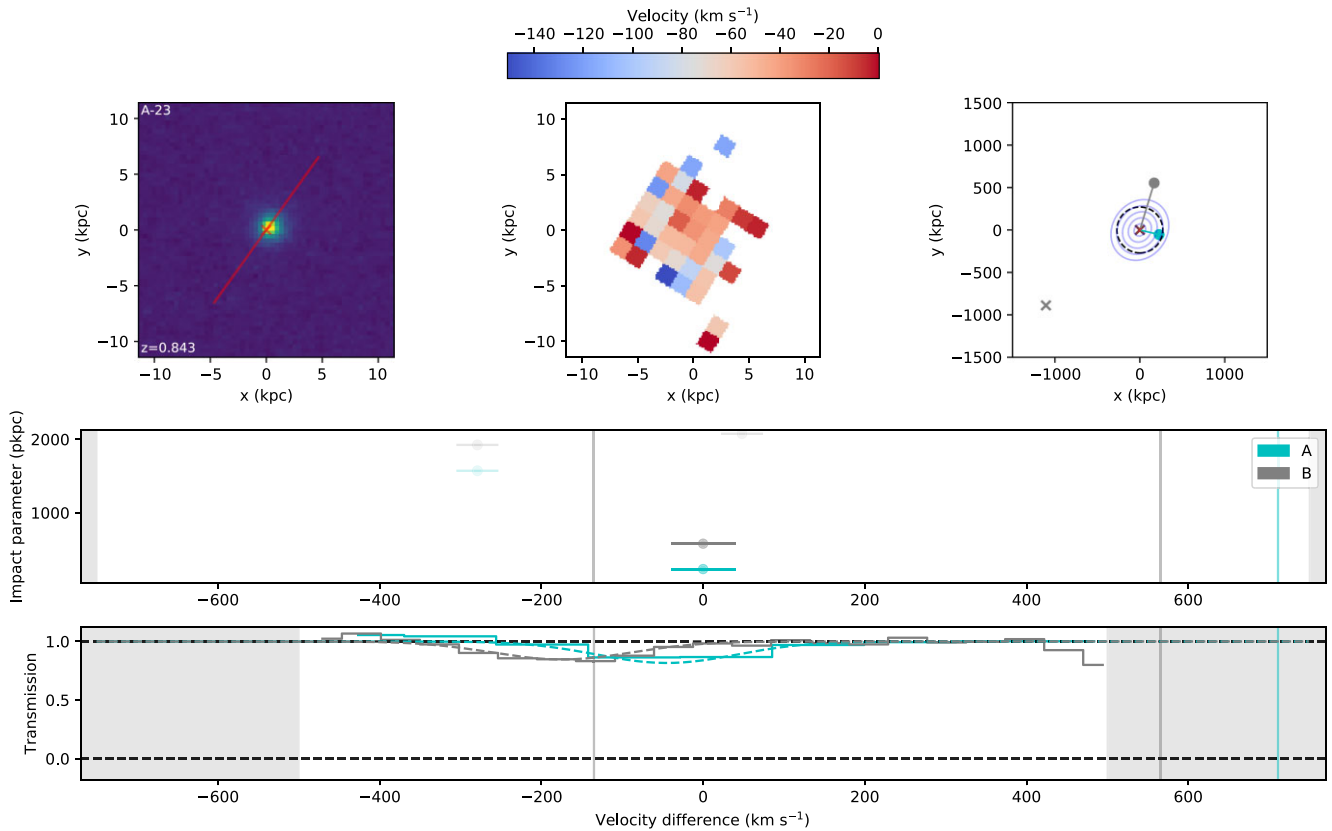


Figure B7. Details of the absorption and galaxy environment around galaxy A-23, a $\sim 0.2L_*$ galaxy at $z \sim 0.84$, using [O II] as observed in MUSE. The layout is identical to that shown in Fig. 3, and the model shown in the lower panel is disc with rotation velocity $\sim 350 \text{ km s}^{-1}$.

thicker disc (height ratio $\sim 30:1$) could, however, produce the absorber in A only, with any weak absorption in B remaining consistent with the observations. This is the model shown in Fig. B9, with a rotation velocity of $\sim 350 \text{ km s}^{-1}$. Reducing the circular velocity and increasing the infall velocity can produce more

reasonable estimates, with $0.6 v_{\text{vir}}$ infall allowing rotation velocities of $\approx 150 \text{ km s}^{-1}$.

Therefore, whilst the absorption in A can be successfully fit with our toy models, we cannot match the major components in A and B simultaneously.

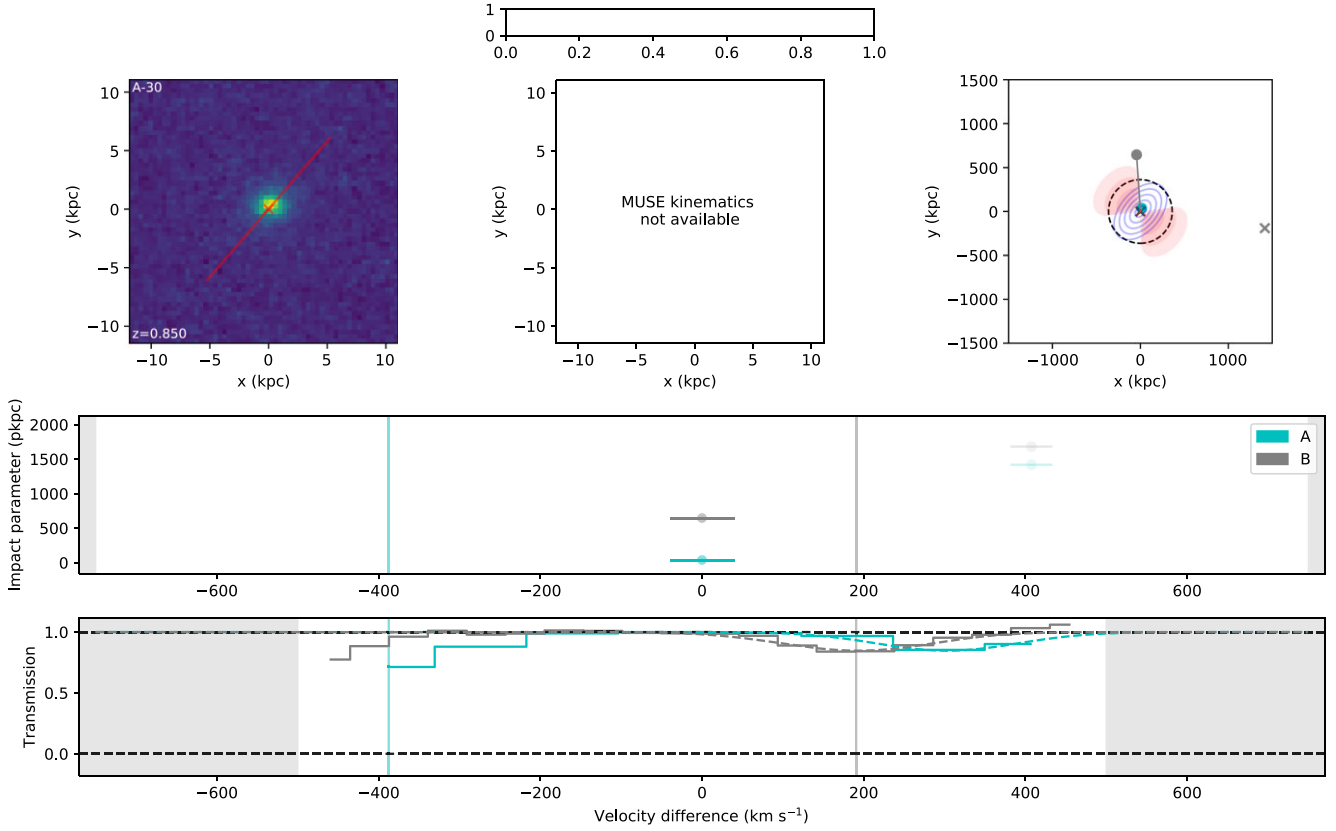


Figure B8. Details of the absorption and galaxy environment around galaxy A-30, a $\sim 0.1L_*$ galaxy at $z \sim 0.85$, using [O II] as observed in MUSE. The layout is identical to that shown in Fig. 3, and the model shown in the lower panel is disc with rotation velocity $\sim 450 \text{ km s}^{-1}$ and outflow with velocity $\sim 250 \text{ km s}^{-1}$.

Table B8. Summary of galaxy-absorber group at $z \sim 0.850$. Any additional galaxies and metal absorbers have velocities shown relative to the first galaxy (A-30). Note that this galaxy is beyond the redshift of QSO-C, so no absorption could be detected. Column descriptions are given in Table 4.

Galaxy	z	Lum (L_*)	Inc	LOS	Imp (kpc)	Azimuth	$\log(N \text{ H I})$	b (km s^{-1})	Δv (km s^{-1})	Other ions
A-30	0.850	0.12 ± 0.02	$53^\circ \pm 9^\circ$	A	39	$19^\circ \pm 11^\circ$	13.71 ± 0.02	106 ± 6	-390 ± 40	-
-	-	-	-	B	647	$45^\circ \pm 11^\circ$	13.32 ± 0.14	70 ± 30	190 ± 40	-

Table B9. Summary of galaxy-absorber group at $z \sim 0.926$. Any additional galaxies and metal absorbers have velocities shown relative to the first galaxy (A-64). Note that this galaxy is beyond the redshift of QSO-C, so no absorption could be detected. Column descriptions are given in Table 4.

Galaxy	z	Lum (L_*)	Inc	LOS	Imp (kpc)	Azimuth	$\log(N \text{ H I})$	b (km s^{-1})	Δv (km s^{-1})	Other ions
A-64	0.926	0.14 ± 0.03	$45^\circ \pm 11^\circ$	A	140	$48^\circ \pm 13^\circ$	14.13 ± 0.13	170 ± 60	140 ± 40	-
-	-	-	-	B	587	$31^\circ \pm 13^\circ$	14.26 ± 0.08	320 ± 70	130 ± 40	-

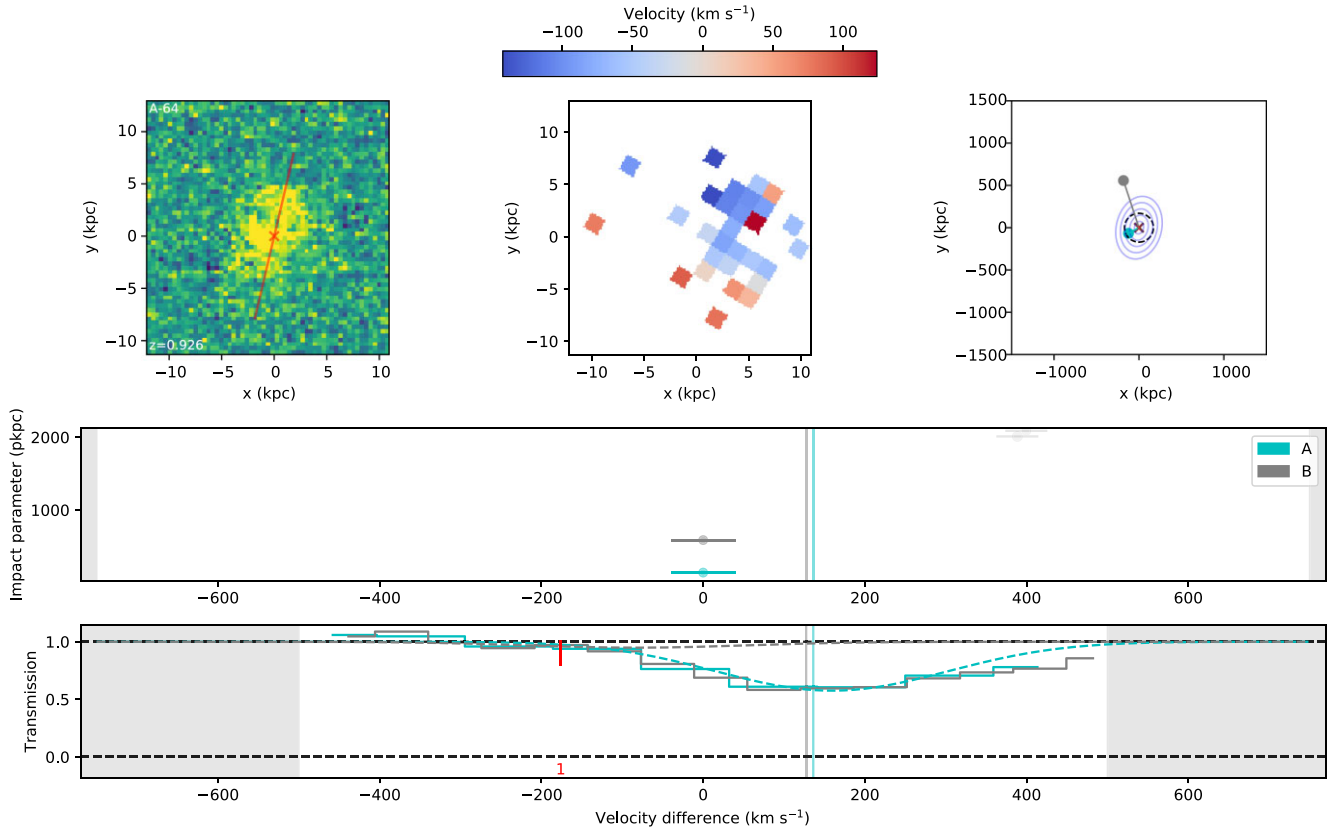


Figure B9. Details of the absorption and galaxy environment around galaxy A-64, a $\sim 0.1L_*$ galaxy at $z \sim 0.93$, using [O II] as observed in MUSE. The layout is identical to that shown in Fig. 3, and the model shown in the lower panel is a disc with rotation velocity $\sim 350 \text{ km s}^{-1}$. The absorption marked in the blue wing in both sightlines is identified as C III from $z = 0.227$.

This paper has been typeset from a $\text{\TeX}/\text{\LaTeX}$ file prepared by the author.